Forschungszentrum Karlsruhe
Technik und Umwelt

Wissenschaftliche Berichte
FZKA 6103

Modelling turbulent dissipation correlations for Rayleigh-Bénard convection based on two-point correlation technique and invariant theory

Q.-Y. Ye, M. Wörner, G. Grötzbach

Institut für Reaktorsicherheit
Projekt Nukleare Sicherheitsforschung

Forschungszentrum Karlsruhe GmbH, Karlsruhe
1998

Abstract

The two-point correlation technique and the invariant theory are used to study the turbulence closure for dissipation correlations in turbulent natural convection. Analytically, an equation for the dissipation rate of turbulence kinetic energy is derived. The structure of this equation is analysed by using direct numerical simulation data (DNS) of turbulent Rayleigh-Bénard convection in air and sodium and of internally heated natural convection. The local homogeneity assumption is found to hold for the two-point velocity correlations and is used to simplify the analytical equation. For the two-point temperature-velocity correlation, on the other hand, it is shown that this assumption is not valid for Rayleigh-Bénard convection.

Using the DNS data, the anisotropy of the Reynolds stresses in natural convection is quantified in the anisotropy invariant map. A new model is proposed for the sink term in the dynamic equation for the dissipation rate which is based on the invariants of the anisotropy tensor of the Reynolds stresses. A model is also proposed for the buoyancy production term, which is of special importance in pure natural convection flows. For the dissipation correlation in the equation for the turbulent heat flux a model is proposed which is consistent with that for the buoyancy production term in the dissipation equation. Both models developed do properly account for wall effects without any explicit wall corrections, but involving only the fluid Prandtl number and the ratio of turbulence thermal to mechanical time scale.

Contents

Nomenclature

a_{ij}	anisotropy tensor of Reynolds stresses, Eq. (5.2)
A_θ	heat flux anisotropy invariant, Eq. (5.27)
D	channel height
D_ϵ	viscous destruction in the dissipation equation, Eq. (4.1)
II	second order invariant, Eq. (5.3)
III	third order invariant, Eq. (5.4)
F	invariant function, Eq. (5.17)
g	gravity
G	buoyancy production in k-equation, Eq. (5.23)
Gr	Grashof number, $Gr = Ra/Pr$ or Eq. (2.5), respectively
J	invariant function, Eq. (5.18)
k	turbulent kinetic energy, $k = \frac{1}{2}\overline{u_i u_i}$
L	invariant function, Eq. (5.19)
p	pressure
q_v	volumetric heat soure
Pe_t	turbulence Peclet number, Eq. (2.7)
Pr	Prandtl number, Eq. (2.2)
P_ϵ^j	production term in the dissipation equation ($j = 1, 2, 3, 4$), Eq. (4.1)
$P_{\epsilon b}$	buoyant production term in the dissipation equation, Eq. (4.5)
R	turbulence time scale ratio, Eq. (5.25)
N_i	number of mesh cells in x_i-direction ($i = 1, 2, 3$)
Ra	Rayleigh number, Eq. (2.1)
Ra_I	internal Rayleigh number, Eq. (2.3)
Re_t	turbulence Reynolds number, Eq. (2.6)
T_b	buoyant production term in the ϵ_h-equation, Eq. (5.1)
T_s	sink term in the ϵ_h-equation, Eq. (5.1)
T_W	wall temperature
U_i	components of the mean velocity ($i = 1, 2, 3$)
u_i	components of the fluctuating velocity ($i = 1, 2, 3$)
u_i'	components of the fluctuating velocity at point B
u_0	velocity scale used for normalisation, $u_0 = (g\beta\Delta T_W D)^{1/2}$
X_i	periodicity length in x_i-direction ($i = 1, 2$)
x_i	coordinates in horizontal ($i = 1, 2$) and vertical ($i = 3$) direction

Greek symbols

α	fluid thermal diffusivity
β	thermal expansion coefficient
δ_{ij}	Kronecker symbol
Δ	Laplace operator ($\Delta_x = \partial^2/\partial x_l \partial x_l$)
ϵ	dissipation rate, Eq. (3.7)
ϵ_h	homogeneous part of the dissipation rate, Eq. (3.7)
ϵ_{ij}	dissipation tensor, Eq. (1.3)
$\epsilon_{ij,h}$	homogeneous part of the dissipation tensor, Eq. (3.6)
$\epsilon_{i\theta}$	dissipation term in the $\overline{u_i\theta}$-equation, Eq. (1.4)
ϵ_θ	dissipation of temperature variance, Eq. (5.26)
θ	fluctuating temperature
Θ	mean temperature
λ	fluid thermal conductivity
ν	fluid kinematic viscosity
ξ_k	coordinate for two-point correlation function
Π_ϵ	pressure term in the ϵ-equation, Eq. (4.1)
ρ	fluid density
τ	mechanical turbulence time scale, $\tau = k/\epsilon$
τ_θ	turbulence thermal time scale, $\tau_\theta = \overline{\theta^2}/(2\epsilon_\theta)$
Υ	viscous destruction in the ϵ-equation, Eq. (4.1)
ψ	coefficient of the sink term in the modeled ϵ-equation, Eq. (5.12)

1 Introduction

Computational fluid dynamics and computational heat and mass transfer are emerging as major tools for solving flow problems encountered in engineering applications. To ensure the physical and technical relevance of the numerical results, reliable modelling of turbulence is of outstanding importance. In the Research Center Karlsruhe for example, the Computer code FLUTAN [25] is developed for single-phase thermo and fluiddynamical problems in two and three dimensions. To extend the field of applicability of the code to flows influenced or dominated by buoyancy, an improved turbulence model for buoyant flows (TMBF [3]) was developed and implemented in the FLUTAN code.

In engineering computer codes, statistical turbulence models based on Reynolds-averaging of the governing instantaneous equations are used to account for the effect of turbulence on flow and heat transfer. In sophisticated statistical turbulence models approximations of the full transport equations for the unknown turbulent stresses and turbulent heat fluxes are solved. In analytical form, the equations describing the evolution of the Reynolds stresses $\overline{u_i u_j}$ and turbulent heat fluxes $\overline{\theta u_i}$ are given by:

$$\begin{aligned}\frac{\partial \overline{u_i u_j}}{\partial t} &+ U_k \frac{\partial \overline{u_i u_j}}{\partial x_k} + \overline{u_j u_k}\frac{\partial U_i}{\partial x_k} + \overline{u_i u_k}\frac{\partial U_j}{\partial x_k} \\ &+ \frac{\partial \overline{u_i u_j u_k}}{\partial x_k} + \frac{1}{\rho}[\overline{u_j \frac{\partial p}{\partial x_i}} + \overline{u_i \frac{\partial p}{\partial x_j}}] + 2\boxed{\nu \overline{\frac{\partial u_i}{\partial x_k}\frac{\partial u_j}{\partial x_k}}} - \nu \Delta_x \overline{u_i u_j} = 0, \end{aligned} \tag{1.1}$$

$$\begin{aligned}\frac{D\overline{\theta u_i}}{Dt} &= \frac{\partial}{\partial x_k}\left\{\alpha \overline{\frac{\partial \theta}{\partial x_k} u_i} + \nu\theta \overline{\frac{\partial u_i}{\partial x_k}} - \overline{\theta u_i u_k}\right\} - \overline{u_i u_k}\frac{\partial T}{\partial x_k} - \overline{\theta u_k}\frac{\partial U_i}{\partial x_k} - g_i \beta \overline{\theta^2} \\ &- \overline{\frac{\theta}{\rho}\frac{\partial p}{\partial x_i}} - \boxed{(\alpha+\nu)\overline{\frac{\partial \theta}{\partial x_k}\frac{\partial u_i}{\partial x_k}}}. \end{aligned} \tag{1.2}$$

The two terms in frames in equations (1.1) and (1.2) represent the dissipation correlations of the Reynolds stresses

$$\epsilon_{ij} = \nu \overline{\frac{\partial u_i}{\partial x_k}\frac{\partial u_j}{\partial x_k}} \tag{1.3}$$

and of the turbulent heat flux rates, respectively:

$$\epsilon_{i\theta} = (\alpha+\nu)\overline{\frac{\partial \theta}{\partial x_k}\frac{\partial u_i}{\partial x_k}}. \tag{1.4}$$

Both, ϵ_{ij} and $\epsilon_{i\theta}$ are unknown. As they represent important sink terms in the above equations, adequate modelling of both dissipation correlations is of special relevance for reliable flow prediction. However, modelling of these dissipation terms is in particular difficult because of a lack of adequate data for the validation of the fundamental closure

assumptions. With the development of advanced numerical simulation techniques, it is nowaday possible to test various closure assumptions directly against a direct numerical simulation (DNS) database. While such databases are even with todays computer power available only for low turbulence intensities, they nevertheless allow for a significant progress towards the development of improved turbulence closures.

Based on the two-point correlation technique, first introduced by Chou [2] and subsequently improved by Kolovandin & Vatutin [15], Ye [32] and Jovanović, Ye & Durst [12] derived analytically an equation describing the dynamics of the dissipation correlation of the Reynolds stresses. They used direct numerical simulation data for a variety of turbulent shear flows to analyse the structure of this equation and to investigate in detail closure assumptions for the dissipation rate.

For flows influenced or dominated by buoyancy it is recognized that turbulence modelling requires special care [8]. The influence of the molecular Prandtl number Pr, the turbulence thermal to mechanical time scale ratio R, and the turbulence Reynolds number Re_t has to be carefully considered in order to obtain accurate and more universal models [26, 28]. While the investigations of Ye [32] and Jovanović et al. [12] are restricted to DNS data for isothermal flows, it appears promising to apply their method to investigate and develop closure assumptions for the turbulent dissipation rate for pure natural convection flows. This is the subject of the present contribution.

In section 2 we present the natural convection flows under investigation, as there are the Rayleigh-Bénard convection and the convection in a horizontal fluid layer heated internally by a volumetric heat source. For Rayleigh-Bénard convection the DNS data of Wörner & Grötzbach [28] for air and sodium are used, while for the internally heated convection the DNS data of Wörner, Schmidt & Grötzbach [22, 30] are utilized. In section 3, the two-point correlation technique is introduced and the dynamic equation which governs the dissipation rate of turbulent kinetic energy in buoyant flows is analysed. In section 4, the assumption of local homogeneity which is used to simplify the derived equation of the dissipation rate is verified for the two-point velocity correlations by use of the DNS data. In section 5, based on the invariant theory introduced by Lumley & Newman [19], new models for the sink term and the buoyant production in the dissipation rate equation are derived. Important parameters of the new models are the fluid Prandtl number and the time scale ratio R. In section 6, the results obtained in section 5 are used to develop a consistent model for the dissipation term $\epsilon_{i\theta}$ in the equation for the turbulent heat fluxes $\overline{u_i\theta}$.

2 Turbulent natural convection

To analyse the structure of the analytically derived equation for the dissipation rate ϵ of turbulence kinetic energy, DNS data of two types of pure natural convection flows are utilized. The flows considered are the Rayleigh-Bénard convection and the convection in an internally heated fluid layer, which are shortly introduced in the next two subsections. Subsequently, some details of the TURBIT computer code and the DNS data are given.

2.1 Rayleigh-Bénard convection

The Rayleigh-Bénard convection is a simple physical model to investigate heat transfer phenomena by natural convection [16]. The fluid is enclosed in an - from a theoretical point of view - infinite horizontal channel which is bounded vertically by two rigid isothermal walls separated by distance D, see Figure 2.1. The lower wall with temperature T_{W1} is heated and the upper wall with temperature T_{W2} is cooled, i.e. $\Delta T_W = T_{W1} - T_{W2} > 0$.

Physically, the Rayleigh-Bénard convection is characterized by two non-dimensional numbers. These are the Rayleigh number

$$Ra = \frac{g\beta\Delta T_W D^3}{\nu\alpha} \tag{2.1}$$

and the Prandtl number

$$Pr = \frac{\nu}{\alpha}. \tag{2.2}$$

Here, ν = kinematic viscosity, α =thermal diffusivity, g =gravity, and β = thermal expansion coefficient. The ratio between Rayleigh number and Prandtl number represents a further dimensionless number, known as the Grashof number $Gr = Ra/Pr$.

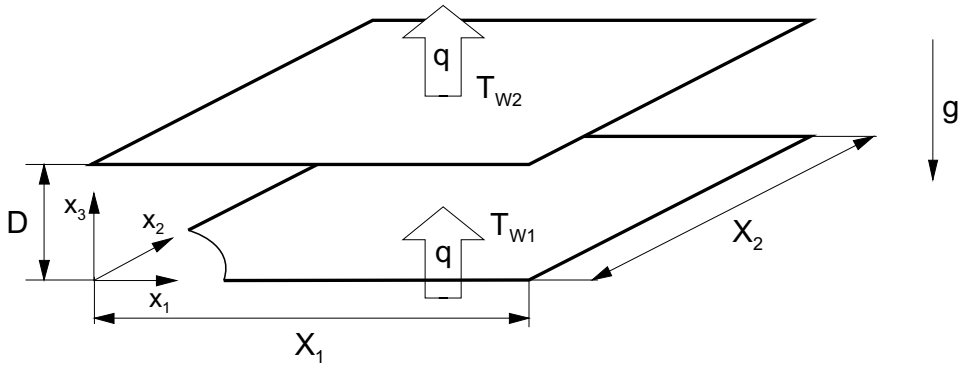

Figure 2.1: Sketch of geometry and heat flux for Rayleigh-Bénard convection.

2.2 Internally heated convection

The natural convection in a horizontal fluid layer which is internally heated by a homogeneous volumetric heat source q_v is of interest to geophysics, to astrophysics, as well as to some special applications of nuclear engineering [17]. The geometry is sketched in Figure 2.2. In the present study, the lower and upper wall are isothermal and obey the same temperature, i.e. $T_{W1} = T_{W2}$. Due to the volumetric heat source the temperature in the layer exceeds the wall temperatures. However, the maximum temperature difference ΔT_{max} across the layer is not known a priori. Therefore, instead of using the Rayleigh number defined by Eq. (2.1) an internal Rayleigh number Ra_I is defined, which does not involve any temperature difference, but is based on the volumetric heat source:

$$Ra_I = \frac{g\beta q_v D^5}{\nu\alpha\lambda}. \tag{2.3}$$

Here, λ is the thermal conductivity. The internal Rayleigh number Ra_I is related to the external Rayleigh number Ra via $Ra_I = Ra/Da$, where Da is the Damköhler number

$$Da = \frac{q_v D^2}{\lambda \Delta T_{max}}. \tag{2.4}$$

Finally, for internally heated convection the definition of the Grashof number is

$$Gr = \frac{Ra_I}{PrDa}. \tag{2.5}$$

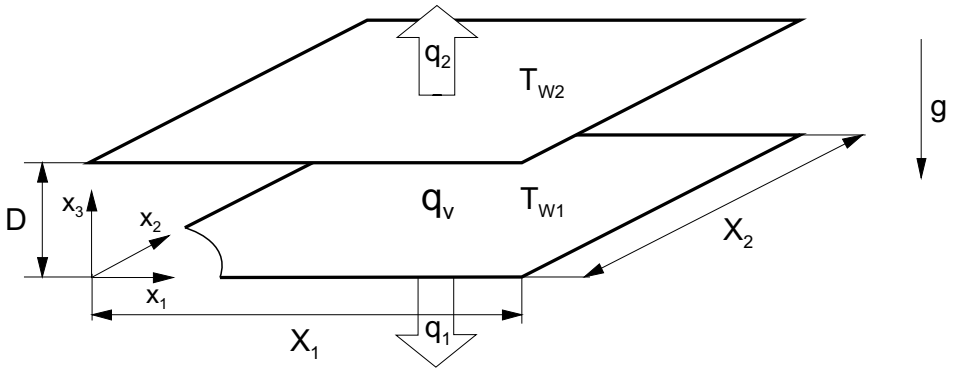

Figure 2.2: Sketch of geometry and heat flux for internally heated natural convection.

2.3 Computer code TURBIT

The results of the direct numerical simulations to be analysed in the present study were computed with the TURBIT code [5]. It solves the three-dimensional time-dependent conservation equations for mass, momentum, and thermal energy for a Newtonian fluid. The formulation is for an incompressible fluid, where the Boussinesq approximation is employed for the buoyancy force. The equations and variables are non-dimensionalised by the following quantities: channel height D, velocity $u_0 = (g\beta\Delta T_w D)^{1/2}$, time D/u_0, pressure ρu_0^2, and temperature difference ΔT_{max}. The discretisation is by a finite volume method, where second order central differences defined on a staggered grid are used for both, the convective and diffusive terms. The time integration method, which involves the solution of a Poisson equation for pressure, is of second order for the convective and of first order for the diffusive terms.

To account for the infinite horizontal extension of a fluid layer, TURBIT allows for the use of periodic boundary conditions in x_1- and x_2-direction. It is important to choose the non-dimensional periodicity length X_1 and X_2 (normalised by D) large enough so that the computational domain covers all the physically relevant macroscopic length scales. On the other hand, in a direct numerical simulation the mesh width must be fine enough to resolve even the smallest scales of turbulence. Details about these mesh requirements, about the initial conditions, the simulation strategy, and the verification of the DNS data by experiments can be found for the simulations of the Rayleigh-Bénard convection in [27] and for the internally heated convection in [22, 30]. In these papers also the patterns and dynamics of the convective layers are discussed in detail.

For the present investigations, statistical quantities evaluated from the three-dimensional time-dependent DNS data are of main interest. Therefore, the averaging procedure used to compute statistical data from the DNS results is shortly explained. For the geometry and boundary conditions used in the direct numerical simulations, statistical data are homogeneous with respect to the horizontal directions. For this reason, the statistical evaluation of a quantity ϕ is performed by ensemble averaging of the DNS data over horizontal planes. In addition, the data are averaged over time. Typically 10 to 40 different datasets are used, each corresponding to a certain problem time. Of course, only such datasets are taken into account for which a steady state of global statistical quantities has been identified.

2.4 Direct numerical simulation data

In the present report DNS data [31] for Rayleigh-Bénard convection in air ($Pr = 0.71$) and sodium ($Pr = 0.006$) at different Rayleigh numbers but similar Grashof numbers are utilized. The relevant parameters of the simulations are listed in Table 2.1, where also one simulation of internally heated convection ($Pr = 7$) is included.

Pr	Ra	Gr	$X_{1,2}$	N_1	N_2	N_3	Re_t	Pe_t
0.006	6,000	10^6	8	200	200	31	497	3
0.006	12,000	2×10^6	8	250	250	39	1081	6.5
0.006	24,000	4×10^6	8	250	250	49	2240	13
0.71	381,000	5.4×10^5	7.92	180	180	32	109	76
0.71	630,000	8.9×10^5	7.92	200	200	49	154	107
	Ra_I							
7	10^8	4.1×10^5	4	160	160	55	4	28

Table 2.1: Simulation parameters for Rayleigh-Bénard convection and internally heated convection.

The DNS results will be used to interprete the turbulent dissipation rate. To quantify the turbulence intensity of the different simulations, in Table 2.1 two dimensionless numbers which are suitable for this purpose are also included. These are the turbulence Reynolds number

$$Re_t = \frac{k^2}{\nu\epsilon} \tag{2.6}$$

and the turbulence Peclet number

$$Pe_t = \frac{k^2}{\alpha\epsilon} = Pr \cdot Re_t, \tag{2.7}$$

where $k = \frac{1}{2}\overline{u_i u_i}$ is the turbulence kinetic energy. The values given in Table 2.1 for Re_t and Pe_t are at channel midwidth, i.e. $x_3 = 0.5$. For liquid sodium the values of the turbulence Reynolds number are quite high. However, the very low values of the turbulence Peclet number indicate that the temperature field is governed by the high thermal conductivity and is predominantly regular. For the internally heated convection Re_t is rather low. Therefore, the DNS results of this simulation will not be used for model development. However, they will be used to check the application range of the models developed on the basis of DNS data for Rayleigh-Bénard convection.

3 Statistical interpretation of the dissipation rate ϵ

The procedure for treating the dissipation correlations is based on the application of the two-point correlation technique that was originally developed by Chou [2] and subsequently refined by Kolovandin & Vatutin [15].

3.1 Two-point correlation technique

A new coordinate system relative to two arbitrary points A and B, as shown in Figure 3.1, is defined in order to separate the effects of local character from the large-scale fluid motions:

$$\xi_k = (x_k)_B - (x_k)_A, \tag{3.1}$$

$$(x_k)_{AB} = \frac{1}{2}[(x_k)_A + (x_k)_B]. \tag{3.2}$$

The partial differential operators at points A and B as function of $(x_k)_{AB}$ and ξ_k are given as follows [10]:

$$\left(\frac{\partial}{\partial x_k}\right)_A = \frac{1}{2}\left(\frac{\partial}{\partial x_k}\right)_{AB} - \frac{\partial}{\partial \xi_k}, \tag{3.3}$$

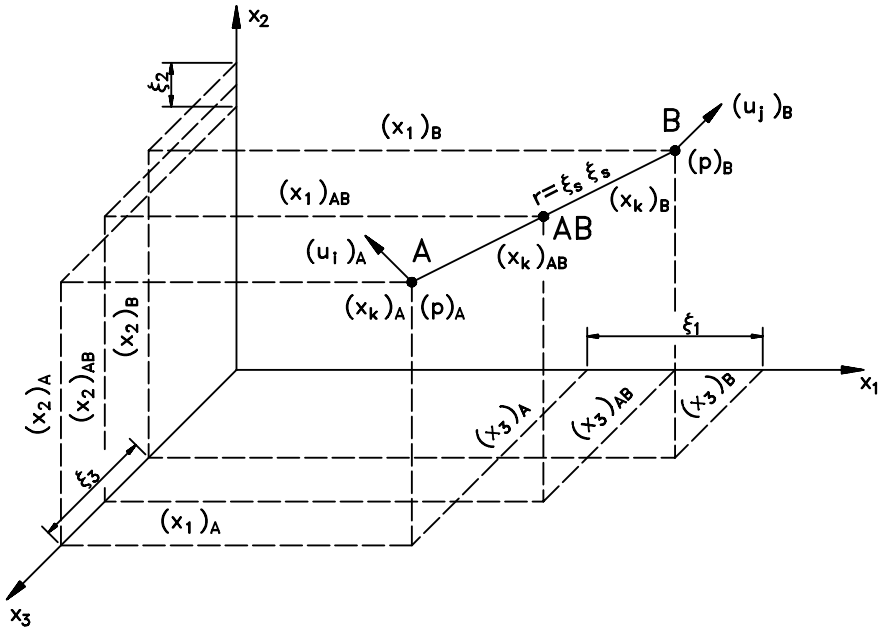

Figure 3.1: Coordinate system used to define the two-point correlation functions.

$$\left(\frac{\partial}{\partial x_k}\right)_B = \frac{1}{2}\left(\frac{\partial}{\partial x_k}\right)_{AB} + \frac{\partial}{\partial \xi_k}, \tag{3.4}$$

$$\left(\frac{\partial}{\partial x_k}\right)_A \left(\frac{\partial}{\partial x_k}\right)_B = \frac{1}{4}\left(\frac{\partial^2}{\partial x_k \partial x_k}\right)_{AB} - \frac{\partial^2}{\partial \xi_k \partial \xi_k}. \tag{3.5}$$

Applying the operator (3.5) to the velocity fluctuation product at two points, $(u_i)_A(u_j)_B$, taking the average and setting ξ_k equal to zero, we obtain:

$$\epsilon_{ij} = \nu\overline{\frac{\partial u_i}{\partial x_k}\frac{\partial u_j}{\partial x_k}} = \frac{1}{4}\nu\Delta_x\overline{u_i u_j} - \nu(\Delta_\xi\overline{u_i u_j'})_0. \tag{3.6}$$

The trace ϵ of this tensor is:

$$\epsilon = \epsilon_{ss} = \nu\overline{\frac{\partial u_s}{\partial x_k}\frac{\partial u_s}{\partial x_k}} = \underbrace{\frac{1}{4}\nu\Delta_x\overline{u_s u_s}}_{inhomogeneous} \underbrace{- \nu(\Delta_\xi\overline{u_s u_s'})_0}_{homogeneous}. \tag{3.7}$$

The prime $'$ in Eq. (3.6) and Eq. (3.7) indicates a value for the two-point correlation function at point B ($\overline{(u_i)_A(u_j)_B} = \overline{u_i u_j'}$) and the subscript $_0$ represents the zero separation $\xi = 0$ between the two points. Equation (3.7) is due to Kolovandin & Vatutin [15].

3.2 Homogeneous and inhomogeneous part of ϵ

According to Eq. (3.6), the tensor ϵ_{ij} is composed of an inhomogeneous part $\frac{1}{4}\nu\Delta_x\overline{u_i u_j}$ and a homogeneous part $-\nu(\Delta_\xi\overline{u_i u_j'})_0$. Jovanović et al. [12] used DNS data of forced turbulent channel flow [20] and computed both parts of ϵ according to Eq. (3.7). The results are given in Figure 3.2, where x_2^+ is the non-dimensional wall distance. It was obtained that the inhomogeneous part of ϵ_{ij} takes a half of the total dissipation rate at the wall and disappears remote from the wall.

In Figures 3.3 - 3.5 we show the vertical distribution of the homogeneous and inhomogeneous part of ϵ calculated from the DNS data for Rayleigh-Bénard convection in air and sodium. Because of the symmetry of the profiles, only the results in the lower half of the channel are shown, i.e. $0 \leq x_3 \leq 0.5$. While the near-wall distribution of the grid points in the direct numerical simulations of the Rayleigh-Bénard convection is fine enough to resolve the viscous and thermal boundary layers, Figures 3.3 - 3.5 show that it is not fine enough to calculate the detailled near-wall behaviour of the terms in Eq. (3.7). Nevertheless, the tendency of the distributions of homogeneous and inhomogeneous part of ϵ for Rayleigh-Bénard convection is similar to that obtained from DNS data for turbulent channel flow. The inhomogeneous part of ϵ_{ij} is of importance near the wall but vanishes far away from the wall.

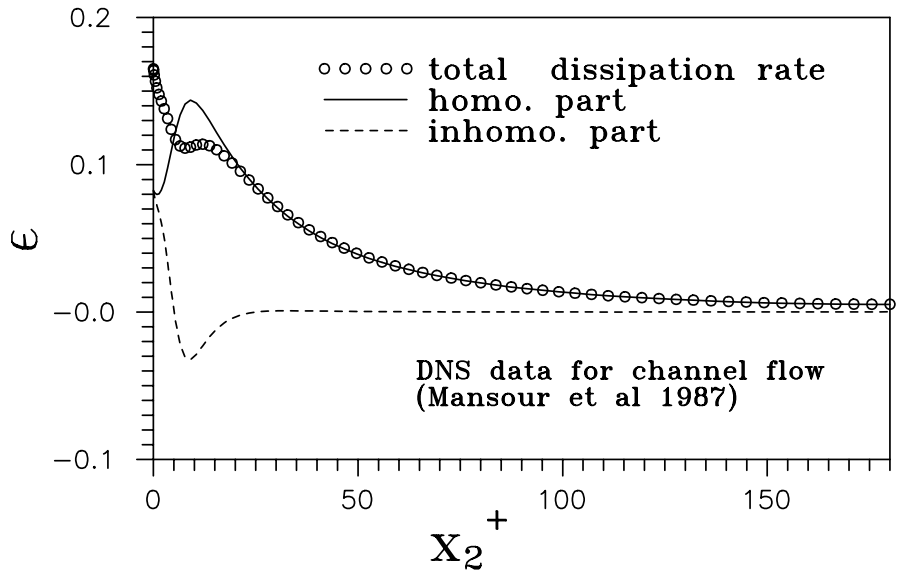

Figure 3.2: Distributions of homogeneous and inhomogeneous part of ϵ. Results of Jovanović et al. [12]. DNS data of forced turbulent channel flow [20].

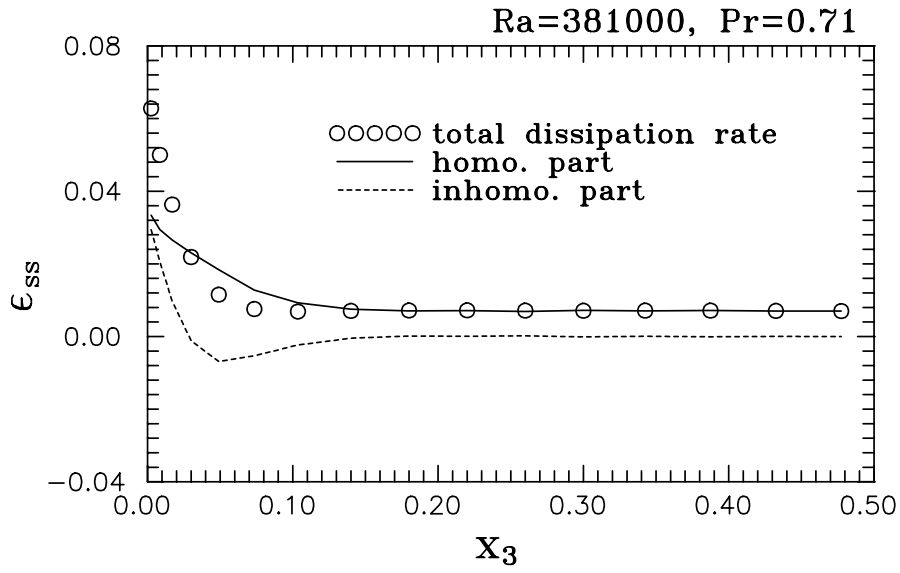

Figure 3.3: Distribution of homogeneous and inhomogeneous part of ϵ. DNS data of Rayleigh-Bénard convection ($Pr = 0.71$, $Ra = 381,000$).

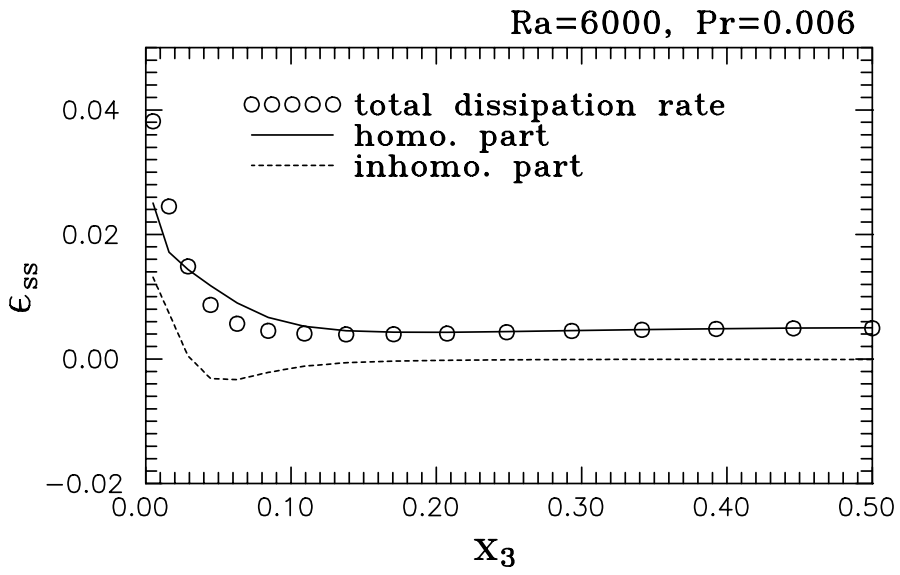

Figure 3.4: Distribution of homogeneous and inhomogeneous part of ϵ. DNS data of Rayleigh-Bénard convection ($Pr = 0.006$, $Ra = 6,000$).

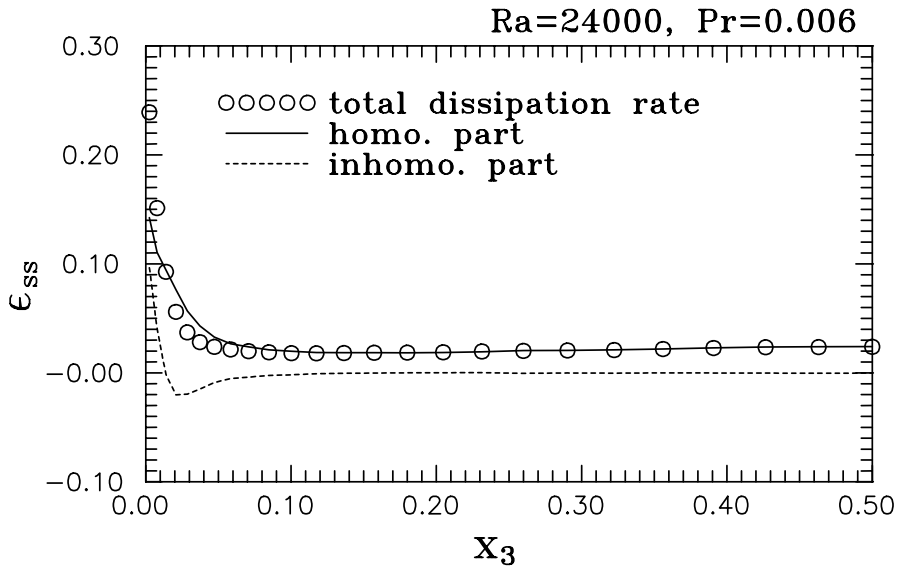

Figure 3.5: Distribution of homogeneous and inhomogeneous part of ϵ. DNS data of Rayleigh-Bénard convection ($Pr = 0.006$, $Ra = 24,000$).

3.3 Wall behaviour of ϵ_{ij}

The wall behaviour of the tensor ϵ_{ij} can be also analysed by expanding a Taylor series near the wall for the instantaneous quantities:

$$\left.\begin{array}{lcllll} u_1 & = & a_1 x_3 & + & a_2 x_3^2 & + \cdots, \\ u_2 & = & b_1 x_3 & + & b_2 x_3^2 & + \cdots, \\ u_3 & = & & & c_2 x_3^2 & + \cdots. \end{array}\right\} \tag{3.8}$$

With the above expansions, the velocity auto-correlations can be written as:

$$\left.\begin{array}{lcllll} \overline{u_1^2} & = & \overline{a_1^2} x_3^2 & + \cdots & + \cdots & + \cdots, \\ \overline{u_2^2} & = & \overline{b_1^2} x_3^2 & + \cdots & + \cdots & + \cdots, \\ \overline{u_3^2} & = & & & \overline{c_2^2} x_3^4 & + \cdots. \end{array}\right\} \tag{3.9}$$

From equation (3.8) and the definition of ϵ_{ij} one obtains for $x_3 \to 0$ the result:

$$\left.\begin{array}{lcllll} \epsilon_{11} & = & \nu\overline{a_1^2} & + \cdots & + \cdots & + \cdots, \\ \epsilon_{22} & = & \nu\overline{b_1^2} & + \cdots & + \cdots & + \cdots, \\ \epsilon_{33} & = & & & 4\nu\overline{c_2^2} x_3^2 & + \cdots, \\ \epsilon_{ss} & = & \nu(\overline{a_1^2} + \overline{b_1^2}) & + \cdots & + \cdots & + \cdots. \end{array}\right\} \tag{3.10}$$

The inhomogeneous part of ϵ near the wall can be read:

$$\frac{1}{4}\nu\Delta_x(\overline{u_s u_s}) = \frac{1}{2}\nu(\overline{a_1^2} + \overline{b_1^2}) + \cdots. \tag{3.11}$$

A comparison of Eq. (3.10) for ϵ_{ss} with Eq. (3.11) reveals that the inhomogeneous part of ϵ contributes to half of the dissipation rate ϵ at the wall. This analytical result confirms the result obtained from the channel flow DNS data for the wall behaviour, shown in Figure 3.2. However, the near wall grid resolution of the DNS data for Rayleigh-Bénard convection is not sufficiently fine to show this wall limiting behaviour, see Figures 3.3 - 3.5.

3.4 Dynamic equation for ϵ_h

As shown in section 3.1, the dissipation correlation ϵ_{ij} of the Reynolds stress $\overline{u_i u_j}$ can be decomposed into two parts. The inhomogeneous part is known by second order turbulence closure. Therefore, we need to consider only the homogeneous part $\epsilon_{ij,h} = -\nu(\Delta_\xi \overline{u_i u_j'})_0$. A dynamic equation for $\epsilon_{ij,h}$ can be derived by applying the operator $\nu\Delta_\xi$ to the dynamic equations for the two point velocity correlation $\overline{(u_i)_A (u_j)_B}$ and taking the limit $\xi_k \to 0$

(see [12]). Since the components of the dissipation tensor ϵ_{ij} can be analytically interpreted in terms of its trace ϵ_{ss} and the second-order velocity correlation $\overline{u_i u_j}$ [2, 15], we are interested only in the contracted form of the equations. It reads as follows:

$$
\begin{aligned}
&-\nu\frac{\partial}{\partial t}(\Delta_\xi\overline{u_s u_s'})_0 - \nu U_k\frac{\partial}{\partial x_k}(\Delta_\xi\overline{u_s u_s'})_0 = \nu[(\Delta_\xi\overline{u_k u_s'})_0 + (\Delta_\xi\overline{u_s u_k'})_0]\frac{\partial U_s}{\partial x_k}\\
&+\frac{\nu}{4}\left[2\overline{u_s u_k}\Delta_x\frac{\partial U_s}{\partial x_k} + (\Delta_x U_k)\frac{\partial}{\partial x_k}\overline{u_s u_s}\right] + \nu\left[\left(\frac{\partial}{\partial\xi_l}\overline{u_s u_k'}\right)_0 - \left(\frac{\partial}{\partial\xi_l}\overline{u_k u_s'}\right)_0\right]\frac{\partial^2 U_s}{\partial x_l\partial x_k}\\
&+2\nu\left(\frac{\partial^2}{\partial\xi_l\partial\xi_k}\overline{u_s u_s'}\right)_0\frac{\partial U_k}{\partial x_l} + \nu\beta g_s[(\Delta_\xi\overline{\theta u_s'})_0 + (\Delta_\xi\overline{u_s\theta'})_0]\\
&+\frac{\nu}{2}\frac{\partial}{\partial x_k}[(\Delta_\xi\overline{u_s u_k u_s'})_0 + (\Delta_\xi\overline{u_s u_s' u_k'})_0]\\
&+\nu[\Delta_\xi\frac{\partial}{\partial\xi_k}(\overline{u_s u_s' u_k'} - \overline{u_s u_k u_s'})]_0 + \frac{\nu}{2\rho}\frac{\partial}{\partial x_s}[(\Delta_\xi\overline{p u_s'})_0 + (\Delta_\xi\overline{u_s p'})_0]\\
&-\frac{\nu}{\rho}[\Delta_\xi\frac{\partial}{\partial\xi_s}(\overline{p u_s'} - \overline{u_s p'})]_0 - \frac{1}{2}\nu^2\Delta_x(\Delta_\xi\overline{u_s u_s'})_0 - 2\nu^2(\Delta_\xi\Delta_\xi\overline{u_s u_s'})_0. \qquad (3.12)
\end{aligned}
$$

Chou [2] has shown that this complicated equation can be simplified, if the assumption of local homogeneity for the small scale structure of turbulence is applied. With this assumption the following properties which are valid for homogeneous turbulence can be used (see [10]):

$$
\begin{aligned}
\overline{u_s u_k'} &= \overline{u_k u_s'}, &(3.13)\\
\overline{u_s u_s' u_k'} &= -\overline{u_s u_k u_s'}, &(3.14)\\
\overline{p u_s'} &= -\overline{u_s p'}. &(3.15)
\end{aligned}
$$

Differentiating equations (3.13) - (3.15) and setting $\xi = 0$, we obtain the following relations:

$$
\begin{aligned}
(\frac{\partial}{\partial\xi}\overline{u_s u_k'})_0 - (\frac{\partial}{\partial\xi}\overline{u_k u_s'})_0 &= 0, &(3.16)\\
(\Delta_\xi\overline{u_s u_s' u_k'})_0 + (\Delta_\xi\overline{u_s u_k u_s'})_0 &= 0, &(3.17)\\
(\Delta_\xi\overline{p u_s'})_0 + (\Delta_\xi\overline{u_s p'})_0 &= 0. &(3.18)
\end{aligned}
$$

Substituting equations (3.16) - (3.18) into Eq. (3.12), we get the approximate equation for the homogeneous part of the dissipation rate $\epsilon_h = -\nu(\Delta_\xi\overline{u_s u_s'})_0$:

$$\frac{\partial \epsilon_h}{\partial t} + U_k \frac{\partial \epsilon_h}{\partial x_k} \simeq 2\nu(\Delta_\xi \overline{u_k u_s'})_0 \frac{\partial U_s}{\partial x_k} + \frac{\nu}{4}\left[2\overline{u_s u_k}\Delta_x \frac{\partial U_s}{\partial x_k} + (\Delta_x U_k)\frac{\partial}{\partial x_k}\overline{u_s u_s}\right]$$
$$+\nu\beta g_s[(\Delta_\xi \overline{\theta u_s'})_0 + (\Delta_\xi \overline{u_s \theta'})_0] + 2\nu\left(\frac{\partial^2}{\partial \xi_l \partial \xi_k}\overline{u_s u_s'}\right)_0 \frac{\partial U_k}{\partial x_l} - 2\nu\left(\Delta_\xi \frac{\partial}{\partial \xi_k}\overline{u_s u_k u_s'}\right)_0$$
$$+\frac{1}{2}\nu\Delta_x \epsilon_h - 2\nu^2(\Delta_\xi \Delta_\xi \overline{u_s u_s'})_0. \tag{3.19}$$

Jovanvović et al. [12] used the DNS data of turbulent channel flow [20] to test the validity of the assumption of locally homogeneous turbulence. They found that away from the wall equation (3.16) and (3.18) can be used. However, the applicability of the assumption of local homogeneity for the second-order derivatives of the triple correlation, Eq. (3.17), could not be justified because of the lack of the appropriate correlations from the simulation database. Hence they kept the term $\frac{\nu}{2}\frac{\partial}{\partial x_k}[(\Delta_\xi \overline{u_s u_k u_s'})_0 + (\Delta_\xi \overline{u_s u_s' u_k'})_0]$ in the governing equation of ϵ_h.

The term $\nu\beta g_s[(\Delta_\xi \overline{\theta u_s'})_0 + (\Delta_\xi \overline{u_s \theta'})_0]$ in Eq. (3.19) accounts for the influence of buoyancy. In isothermal flows, this term does not appear and thus it was not considered in [12]. For homogeneous turbulence, similar to Eq. (3.15) and Eq. (3.18) the relations

$$\overline{\theta u_s'} = -\overline{u_s \theta'} \tag{3.20}$$

and

$$(\Delta_\xi \overline{\theta u_s'})_0 + (\Delta_\xi \overline{u_s \theta'})_0 = 0 \tag{3.21}$$

should hold. Thus, provided that the assumption of local homogeneity for small scales of turbulence is also valid for two-point temperature-velocity correlations, the above buoyancy term should vanish. In the next section, the DNS data for turbulent Rayleigh-Bénard convection will be used to test the validity of the assumption of locally homogeneous turbulence for both, the two-point velocity correlations of third rank and the two-point temperature-velocity correlations.

4 Validation of the approximate equation for ϵ_h

In section 3, the assumption of local homogeneity was introduced in order to simplify the derived equation for ϵ_h. However, the validity of this assumption for the Rayleigh-Bénard convection has still to be shown. In particular, there are two main open questions which need to be clarified and which will be addressed in this section by utilizing the DNS data for Rayleigh-Bénard convection. These questions concern the validity of the assumption of local homogeneity for the derivatives of (i) two-point velocity correlations of third rank and (ii) of two-point temperature-velocity correlations. To perform this task, we first give the exact transport equation for ϵ derived from the Navier-Stokes equations [24]:

$$\begin{aligned}\frac{D\epsilon}{Dt} = & \underbrace{-2\nu\overline{\frac{\partial u_i}{\partial x_l}\frac{\partial u_k}{\partial x_l}\frac{\partial U_i}{\partial x_k}}}_{P_\epsilon^1}\underbrace{-2\nu\overline{\frac{\partial u_i}{\partial x_k}\frac{\partial u_i}{\partial x_l}\frac{\partial U_k}{\partial x_l}}}_{P_\epsilon^2}\underbrace{-2\nu\overline{u_k\frac{\partial u_i}{\partial x_l}\frac{\partial^2 U_i}{\partial x_k\partial x_l}}}_{P_\epsilon^3} \\ & \underbrace{-2\nu\overline{\frac{\partial u_i}{\partial x_l}\frac{\partial u_k}{\partial x_l}\frac{\partial u_i}{\partial x_k}}}_{P_\epsilon^4}\underbrace{-2\nu\beta g_i\overline{\frac{\partial\theta}{\partial x_l}\frac{\partial u_i}{\partial x_l}}}_{P_{\epsilon b}}\underbrace{-\nu\frac{\partial}{\partial x_k}[\overline{u_k\frac{\partial u_i}{\partial x_l}\frac{\partial u_i}{\partial x_l}}]}_{T_\epsilon} \\ & \underbrace{-\frac{2\nu}{\rho}\overline{\frac{\partial u_i}{\partial x_l}\frac{\partial^2 p}{\partial x_i\partial x_l}}}_{\Pi_\epsilon}\underbrace{-2\nu^2\overline{\frac{\partial^2 u_i}{\partial x_l\partial x_n}\frac{\partial^2 u_i}{\partial x_l\partial x_n}}}_{\Upsilon}\underbrace{+\nu\Delta_x\epsilon}_{D_\epsilon}. \end{aligned} \tag{4.1}$$

In Eq. (4.1), the terms P_ϵ^1 - P_ϵ^4 belong to the production of ϵ. The other terms on the right-hand side of Eq. (4.1) represent the buoyancy production $P_{\epsilon b}$, the turbulent diffusion $(T_\epsilon + \Pi_\epsilon)$, the viscous destruction Υ of ϵ, and the viscous diffusion D_ϵ. In section 4.3, these terms are computed from the direct numerical simulation data and the results are used to analyse the contribution of each term in the approximate equation for ϵ_h.

4.1 Two-point velocity correlations of third rank

In order to determine the applicability of the local homogeneity assumption for the derivatives of two-point velocity correlations of the third rank, i.e. to test the validity of

$$(\Delta_\xi\overline{u_s u_k u_s'})_0 + (\Delta_\xi\overline{u_s u_s' u_k'})_0 \simeq 0, \tag{4.2}$$

the following correlation is considered by means of the two-point correlation technique:

$$\nu\frac{\partial}{\partial x_k}\overline{\frac{\partial u_i}{\partial x_l}\frac{\partial u_k u_i}{\partial x_l}} = \frac{1}{4}\nu\frac{\partial}{\partial x_k}\Delta_x\overline{u_i u_k u_i} - \frac{1}{2}\nu\frac{\partial}{\partial x_k}[(\Delta_\xi\overline{u_i' u_k u_i})_0 + (\Delta_\xi\overline{u_i u_k' u_i'})_0]. \tag{4.3}$$

If the assumption of local homogeneity is valid, equation (4.3) can be approximated as follows:

$$\underbrace{\nu\frac{\partial}{\partial x_k}\overline{\frac{\partial u_i}{\partial x_l}\frac{\partial u_k u_i}{\partial x_l}}}_{T_l} \simeq \underbrace{\frac{1}{4}\nu\frac{\partial}{\partial x_k}\Delta_x\overline{u_i u_k u_i}}_{T_r}. \tag{4.4}$$

Figure 4.1 shows the comparison between the two terms T_l and T_r in Eq. (4.4). The result supports the validity of the approximation given by Eq. (4.4) except for a few points in the vicinity of the wall.

4.2 Two-point temperature-velocity correlations

Using the two-point correlation technique, the buoyant production $P_{\epsilon b}$ of ϵ can be written as

$$P_{\epsilon b} = -2\nu\beta g_i \overline{\frac{\partial\theta}{\partial x_l}\frac{\partial u_i}{\partial x_l}} = -\frac{1}{2}\nu\beta g_i \Delta_x \overline{\theta u_i} + \nu\beta g_i[(\Delta_\xi \overline{\theta u_i'})_0 + (\Delta_\xi \overline{u_i\theta'})_0]. \tag{4.5}$$

If the temperature-velocity correlation is locally homogeneous, then

$$(\Delta_\xi \overline{\theta u_i'})_0 + (\Delta_\xi \overline{u_i\theta'})_0 \simeq 0 \tag{4.6}$$

and $P_{\epsilon b}$ can be approximated as

$$P_{\epsilon b} \simeq -\frac{1}{2}\nu\beta g_i \Delta_x \overline{\theta u_i}. \tag{4.7}$$

The DNS data of Rayleigh-Bénard convection with the largest turbulence Peclet number, i.e. air with $Ra = 630,000$ and $Pe_t = 107$ at $x = 0.5$, are chosen to test approximation (4.7). Figure 4.2 shows a comparison between the data for $P_{\epsilon b}$ obtained from the direct numerical simulation and the right-hand side of relation (4.7). It appears that the assumption of local homogeneity for the two-point temperature-velocity correlations is not applicable here. This is probably due to the rather low value of the turbulence Peclet number. However, while the turbulence Reynolds number is only a factor $Pr^{-1} \approx 1.4$ higher than Pe_t, the statistical state of the small structure of the velocity field is, at least away from the wall, found to be locally homogeneous (see section 4.1).

4.3 Budget of the approximate equation for ϵ_h

As a result of the analysis in section 4.1, the derivatives of the two-point velocity correlations of third rank are neglected in Eq. (3.19). Those are usually interpreted as the turbulent transport in the ϵ equation. The derivatives of the two-point temperature-velocity correlation in Eq. (3.19), however, are kept because the assumption of local homogeneity is not valid for this term. From the DNS data, all terms in the transport equation for ϵ, Eq. (4.1), and for ϵ_h, Eq. (3.19), can be computed. The budgets gained by this procedure for the DNS data of Rayleigh-Bénard convection in air ($Ra = 381,000$) are shown in Figure 4.3 (a,b) for Eq. (4.1) and for Eq. (3.19), respectively. With exception of the first few grid points close to the wall, the derived equation (3.19) balances the data reasonably well.

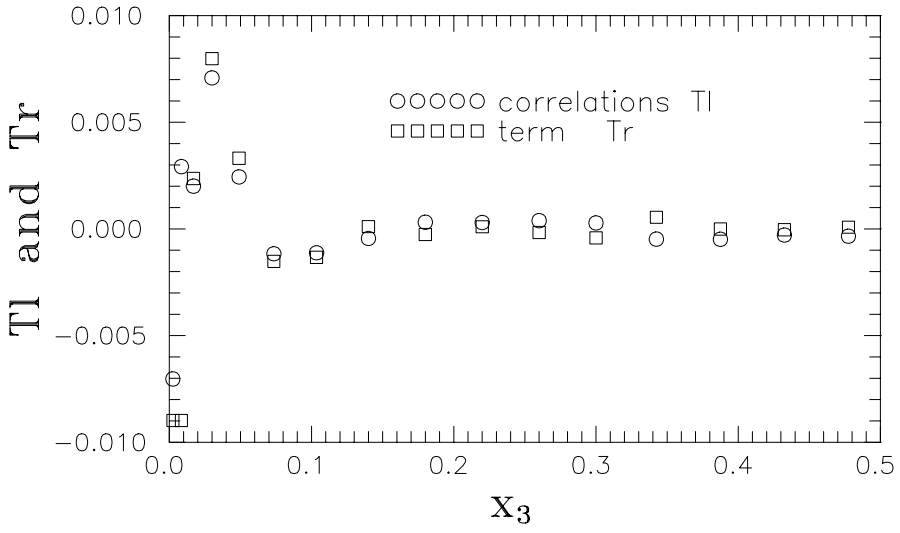

Figure 4.1: Distribution of correlation T_l and T_r computed from the DNS data for Rayleigh-Bénard convection in air ($Ra = 381,000$, $Pr = 0.71$).

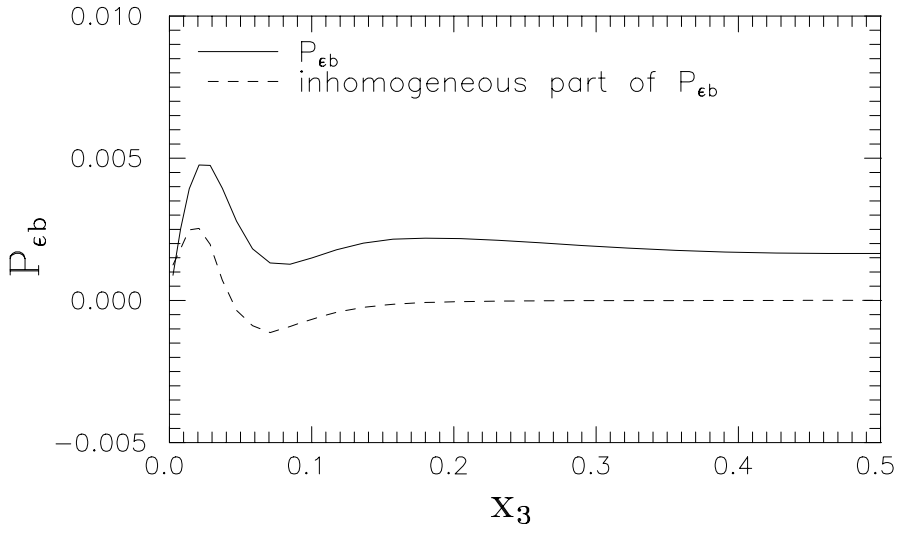

Figure 4.2: Distribution of $P_{\epsilon b}$ and right-hand side of Eq. (4.7) computed from the DNS data for Rayleigh-Bénard convection in air ($Ra = 630,000$, $Pr = 0.71$).

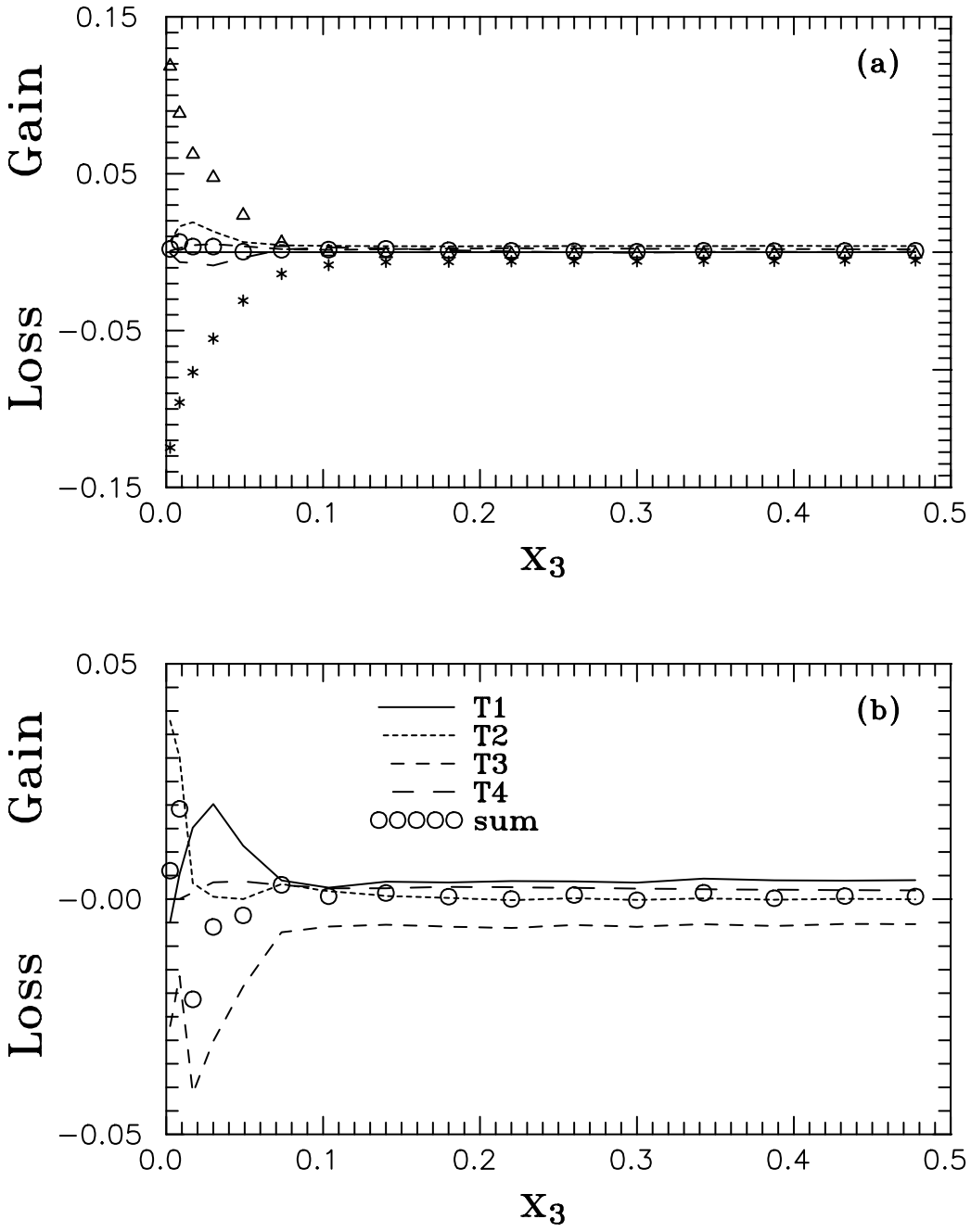

Figure 4.3: Budget computed from DNS data ($Ra = 381,000$, $Pr = 0.71$). (a) Budget of ϵ Eq. (4.1): ——, $P^1_\epsilon + P^2_\epsilon + P^3_\epsilon$; ---, P^4_ϵ; – – –, $P_{\epsilon b}$; ———, $T_\epsilon + \Pi_\epsilon$; $\triangle$, D_ϵ; $*$, $-\Upsilon$; $\circ$, sum of all terms. (b) Budget of Eq. (3.19): ——, $T1 = -2\nu[\Delta_\xi(\partial/\partial\xi_k)(\overline{u_s u_k u'_s})]_0$; ---, $T2 = 1/2\nu\Delta_x\epsilon_h$; – – –, $T3 = -2\nu^2(\Delta_\xi\Delta_\xi\overline{u_s u'_s})_0$; ———, $T4 = \nu\beta g_s[(\Delta_\xi\overline{\theta u'_s}) + (\Delta_\xi\overline{u_s\theta'})]$; $\circ$, sum of all terms.

5 Modelling of the approximate equation for ϵ_h

In fully developed turbulent Rayleigh-Bénard convection the long-time averaged mean velocity is zero, i.e. $U_i = 0$. As a consequence, in the approximate equation (3.19) for the homogeneous part of the turbulent dissipation rate all terms containing U_i drop out, and the equation simplifies to the form

$$\frac{\partial \epsilon_h}{\partial t} \simeq \underbrace{\nu\beta g_s[(\Delta_\xi \overline{\theta u_s'})_0 + (\Delta_\xi \overline{u_s \theta'})_0]}_{T_b} \underbrace{-2\nu^2(\Delta_\xi \Delta_\xi \overline{u_s u_s'})_0 - 2\nu\left(\Delta_\xi \frac{\partial}{\partial \xi_k}\overline{u_s u_k u_s'}\right)_0}_{T_s} + \frac{1}{2}\nu\Delta_x \epsilon_h. \tag{5.1}$$

In this section, models for the two remaining important closure terms for pure natural convection will be developed, as there are (i) the sink term T_s and (ii) the buoyant production term T_b. To prepare the development of these models, in the next subsection we first give an introduction to the invariant theory, and subsequently present the new models.

5.1 Anisotropy invariant map

In order to quantify the anisotropy and to define the state of turbulence, Lumley & Newmann [19] introduced the anisotropy tensor for the Reynolds stresses

$$a_{ij} = \frac{2\overline{u_i u_j}}{k} - \frac{1}{3}\delta_{ij} \tag{5.2}$$

and its second and third scalar invariants

$$II = a_{ij}a_{ji}, \tag{5.3}$$
$$III = a_{ij}a_{ik}a_{jk}. \tag{5.4}$$

Here, $k = \frac{1}{2}\overline{u_s u_s}$ is the turbulent kinetic energy and δ_{ij} is the Kronecker delta tensor. The relationships between II and III are for axisymmetric turbulence

$$II = \frac{3}{2}(\frac{4}{3}|III|)^{2/3} \tag{5.5}$$

and for two-component turbulence

$$II = \frac{2}{9} + 2III. \tag{5.6}$$

By both invariants the anisotropy invariant map (AIM) is defined, as shown in Figure 5.1. In the AIM, all physically realizable turbulence is defined [18].

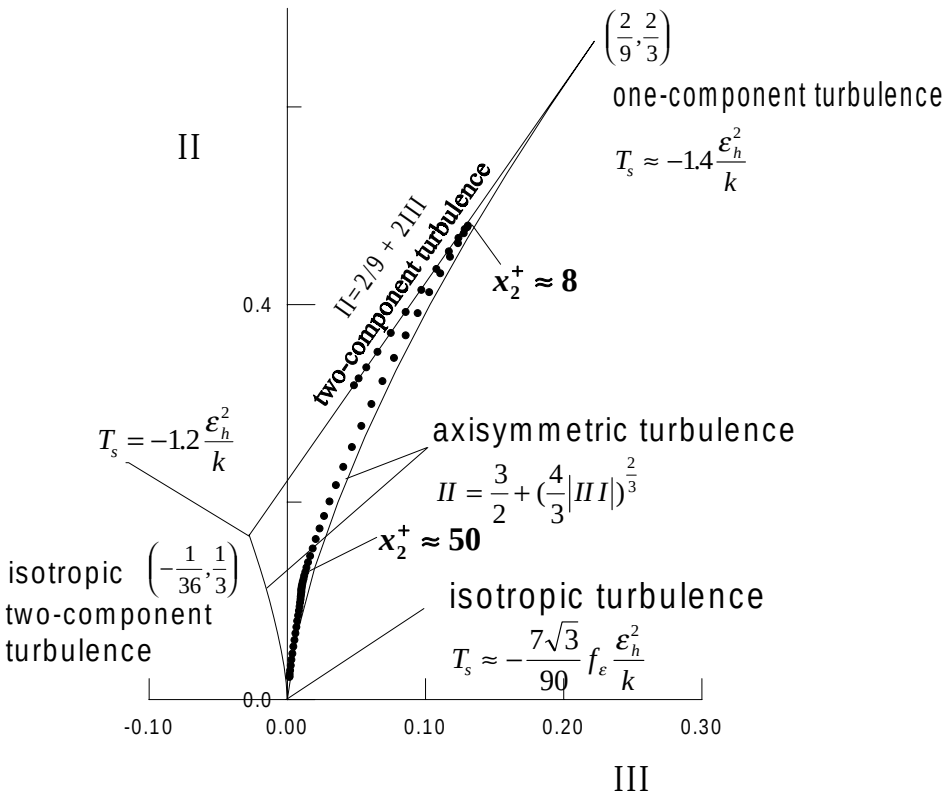

Figure 5.1: Anisotropy invariant map of Reynolds stress. •, DNS data for forced channel flow (Mansour et al. 1988). $Re_t \simeq 240$ in the channel center.

Using the DNS data for turbulent channel flow [20] and the present DNS data for Rayleigh-Bénard convection, the anisotropy invariant maps for a_{ij} are shown in Figures 5.1 - 5.3. In these figures, each marker corresponds to a certain wall distance x_2^+ or x_3, respectively. The upper boundary of the AIM is described by Eq. (5.6) and characterises two-component turbulence, where one velocity component is zero. Invariants corresponding to positions very close to the wall locate near this boundary. In this case, the Reynolds stress component normal to the wall is negligible near the wall. The right-hand and left-hand boundaries of the AIM represent axisymmetric turbulence. With increasing wall distance, the data of the invariants follow these boundaries and tend towards isotropic turbulence (i.e. $II = III = 0$) in the center of the channel.

For Rayleigh-Bénard convection in air, the anisotropy invariant map is shown in Figure 5.2 for the two different Rayleigh numbers, $Ra = 381,000$ and $Ra = 630,000$. Starting close the wall ($x_3 \approx 0$), the invariants II and III follow the left-hand boundary of the AIM. For $x_3 \approx 0.2$ (and $x_3 \approx 0.8$, respectively) II and III are almost zero, and thus the turbulence is almost isotropic. With further increase of the wall distance $x_3 \to 0.5$,

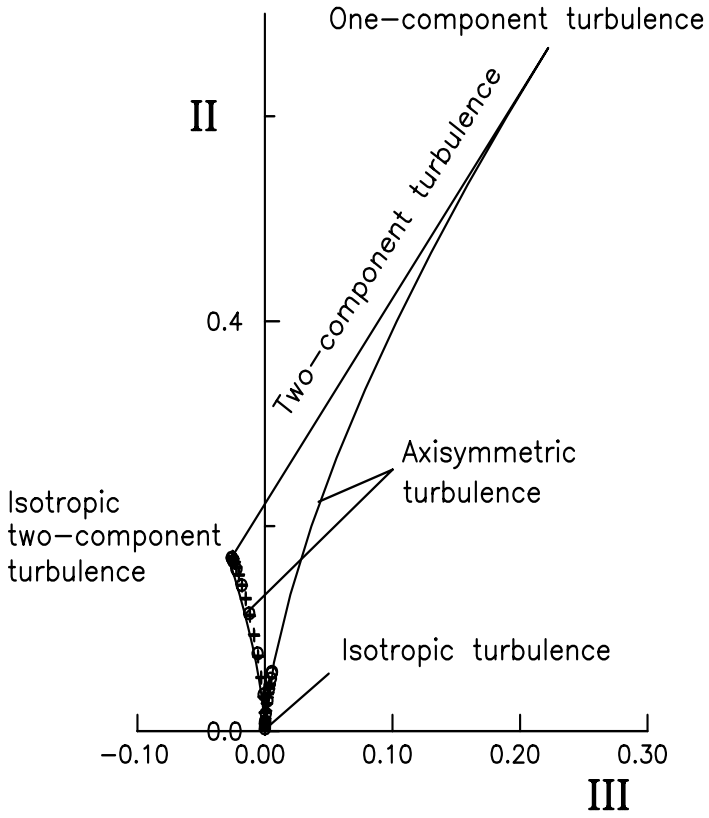

Figure 5.2: Anisotropy invariant map for Rayleigh-Bénard convection in air ($Pr = 0.71$). ○: $Ra = 381,000$ ($Re_t = 109$); +:, $Ra = 630,000$ ($Re_t = 154$).

the invariants change their location in the AIM and now follow the right-hand boundary.

The invariants for Rayleigh-Bénard convection in liquid sodium are shown in Figure 5.3 for the Rayleigh numbers $Ra = 6,000$ and $Ra = 12,000$. For positions away from the wall, the invariants locate near the right-hand boundary of the AIM. In general, the invariants reside near the right-hand boundary of the AIM, if two of the components of $\overline{u_i u_j}$ are nearly equal while the third one is larger. For the left-hand boundary, the third component is smaller while the other two components are about equal.

To explain the location of the invariants II and III in the AIM for Rayleigh-Bénard convection in air and sodium, we have to discuss statistics of the velocity field and mechanims of the convective heat transfer. In Rayleigh-Bénard convection in air at the Rayleigh numbers considered, the vertical profiles of $\overline{u_1^2}$ and $\overline{u_2^2}$ are almost identical, and the trace components of the Reynolds stress tensor behave as $\overline{u_1^2} \approx \overline{u_2^2} > \overline{u_3^2}$ in the range $0 < x_3 < 0.2$ and $0.8 < x_3 < 1$, while in the center of the channel $\overline{u_3^2} > \overline{u_1^2} \approx \overline{u_2^2}$ (see page 78 in [27]). This is because in the simulations for Rayleigh-Bénard convection in air

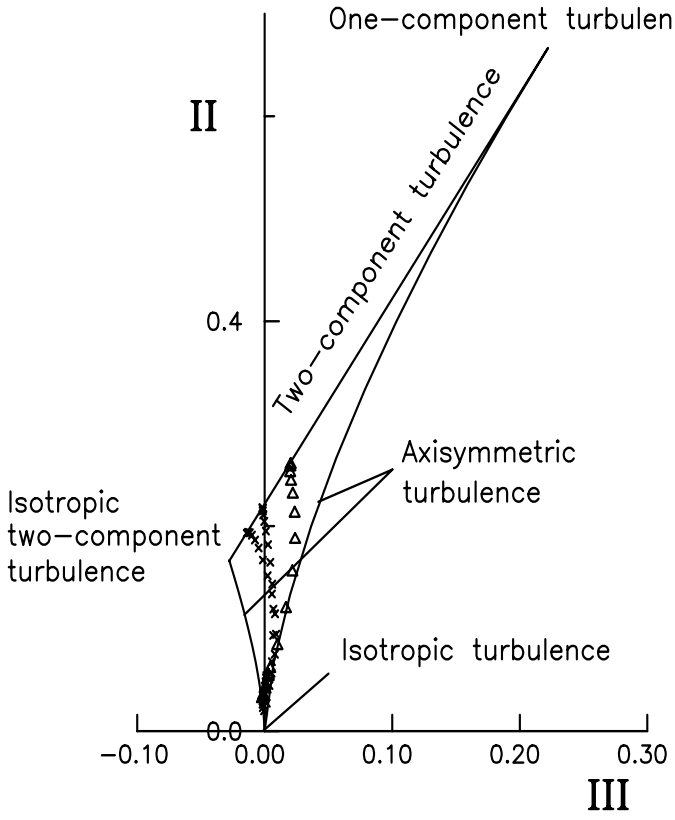

Figure 5.3: Anisotropy invariant map for Rayleigh-Bénard convection in sodium ($Pr = 0.006$). $\triangle$: $Ra = 6,000$ ($Re_t = 497$); $\times$: $Ra = 12,000$ ($Re_t = 1081$).

the heat transfer is dominated by plumes, which intermittently release from the unstably stratified thermal boundary layers at the top and bottom wall. After release from the top or bottom wall, respectively, the plumes are accelerated in the isothermal core region by buoyancy forces and eventually penetrate the boundary layer at the opposite wall with high kinetic energy. There, due to the presence of the wall, the fluid is redistributed horizontally. The dynamics and convective structures are discussed in detail in [7].

For Rayleigh-Bénard convection in liquid sodium at $Ra = 12,000$ in contrary, there are still remainders of regular two-dimensional convection rolls [7], typical for slightly supercritical Rayleigh-Bénard convection. However, superimposed to these large scale vortex bands are highly turbulent small scales. For this reason, other than in air, the horizontal velocity components are at those small value of Ra not yet isotropic and the vertical profiles of $\overline{u_1^2}$ and $\overline{u_2^2}$ substantially differ in sodium, as well as they differ from $\overline{u_3^2}$ [27]. For Rayleigh-Bénard convection in sodium, therefore, the anisotropy of the velocity field as shown in the AIM is higher than that for air.

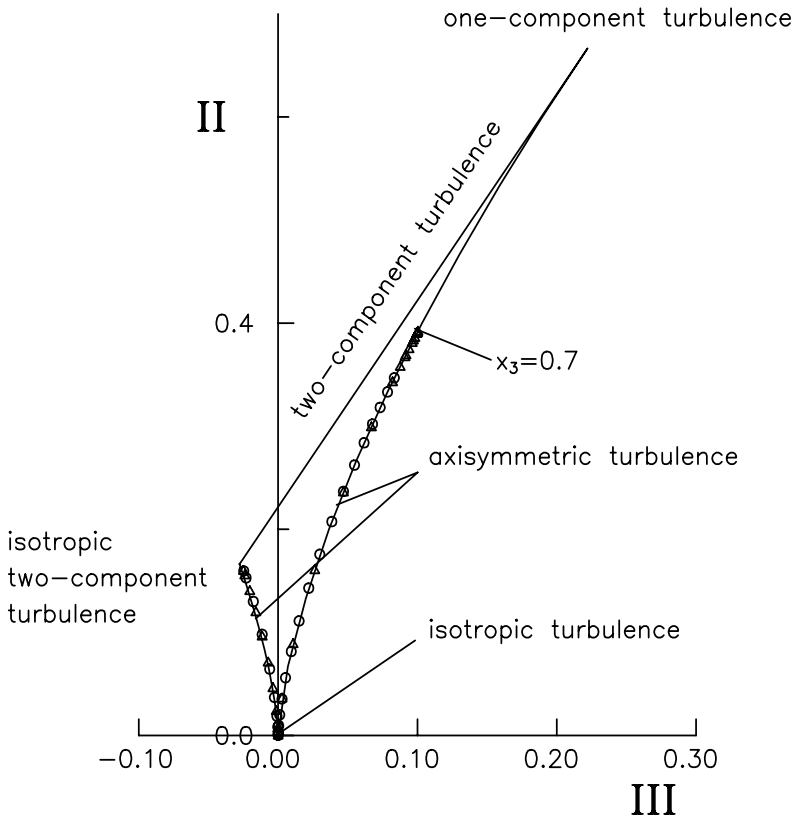

Figure 5.4: Anisotropy invariant map of Reynolds stress for internally heated convection ($Pr = 7$). $Ra_I = 10^8$, $Re_t = 4$; $\circ$, $0 < x_3 < 0.5$; $\triangle$, $0.5 < x_3 < 1$.

Comparing the anisotropy invariant map of forced convection (Fig. 5.1) and Rayleigh-Bénard convection (Fig. 5.2 and 5.3), one observes that the anisotropy of the Reynolds stress tensor for Rayleigh-Bénard convection is smaller than that for forced convection in both the near wall and buffer region. This is expected, since there is no mean strain in turbulent natural convection.

In Figure 5.4, we show the AIM for the DNS data of internally heated convection. For vertical positions close to the wall $0 < x_3 < 0.1$ and $0.9 < x_3 < 1$, the invariants II and III locate on the left-hand boundary of the AIM. In the center of the channel, $0.1 < x_3 < 0.9$, the anisotropy increases till $x_3 \approx 0.7$ where it is maximal, and decreases with further increase of x_3. Note that in contrast to the Rayleigh-Bénard convection for internally heated convection the flow and temperature field is not symmetric to the channel center line [22, 30]. Nevertheless, the behaviour in the AIM described is quite similar to that for Rayleigh-Bénard convection in air (Figure 5.2).

Antonia et al. [1] argued that there is no discernible Reynolds-number effect on the turbu-

lence states indicated by anisotropy invariant maps. However, the turbulence Reynolds numbers they considered were not too different ($Re_t \approx 240$ and $Re_t \approx 390$). Paying attention to Re_t in Figure 5.1 and Figure 5.3 it seems that for low turbulent Reynolds numbers the invariants near the wall reside more close to the one-component turbulence (the maximal physically possible value for II and III). Although this conclusion can not be supported by Figure 5.2, the AIM in Figure 5.2 is quite different from that in Figures 5.1 and 5.3. However, if one compares the invariants in the region of the channel center from Fig. 5.2 and Fig. 5.4, a turbulence Reynolds-number effect does exist. A more detailed investigation should be carried out in the future to clarify this topic.

5.2 Model for the sink term

The appropriate modelling of the sink term in the dissipation rate equation is very important, since it is one of the dominant terms. Using the invariant theory [19] and the DNS data of turbulent channel flow at a small Reynolds number, the closure for the sink term T_s in Eq. (5.1) was investigated in detail by Ye [32]. An equivalent method is used here, however, for DNS data of pure natural convection.

Some limiting values of T_s at different turbulent states, which were deduced by different researchers, were utilized in [32] to construct a model for T_s which is valid across the entire anisotropy invariant map. These limiting values are

$$(T_s)_{1C} = -1.4\frac{\epsilon_h^2}{k} \tag{5.7}$$

for one-component turbulence [19],

$$(T_s)_{2C} = -0.0517\sqrt{20Re_t}\frac{\epsilon_h^2}{k} \tag{5.8}$$

for two-component turbulence,

$$(T_s)_{iso} = -7\frac{\sqrt{3}}{90}f_\epsilon\frac{\epsilon_h^2}{k} \tag{5.9}$$

for isotropic turbulence, and

$$(T_s)_{2C-iso} = -1.2\frac{\epsilon_h^2}{k} \tag{5.10}$$

for two-component isotropic turbulence (see [32]). The model for the sink term in the entire AIM is now, similar to [32], constructed by superposition of the sink term models for two-component turbulence $(T_s)_{2C}$ and axisymmetric turbulence $(T_s)_{axi}$

$$T_s = (1-F)(T_s)_{2C} + F(T_s)_{axi} = -\psi\frac{\epsilon_h^2}{k}. \tag{5.11}$$

The coefficient

$$\psi = (1-F)\psi_{2C} + F\psi_{axi} = \psi(Re_t, II, III) \tag{5.12}$$

is given by

$$\psi_{2C} = [0.02 + 0.03\exp(-Re_t)]\sqrt{20Re_t} \tag{5.13}$$

$$\psi_{axi} = 1.4 + L(\frac{7\sqrt{3}}{90}f_\epsilon - 1.4), \quad III > 0 \tag{5.14}$$

$$\psi_{axi} = 1.2 + L(\frac{7\sqrt{3}}{90}f_\epsilon - 1.2). \quad III < 0. \tag{5.15}$$

Here, the decay function f_ϵ proposed by Coleman & Mansour [4] is used:

$$f_\epsilon = \frac{54\sqrt{3}}{7}[1 - 0.222\exp(-0.336\sqrt{Re_t})]. \tag{5.16}$$

The parameter F equals unity when the stress field is axisymmetric while it is zero in two-component turbulence [32]:

$$F = \frac{J^2}{L} \quad \begin{cases} F = 0, & \text{by two-component-turbulence} \\ F = 1, & \text{by axisymmetric and isotropic turbulence} \end{cases} \tag{5.17}$$

$$J = 1 - 9(\frac{1}{2}II - III), \tag{5.18}$$

$$L = 1 - 9[\frac{3}{4}(\frac{4}{3}|III|)^{2/3} - III]. \tag{5.19}$$

It is found that the function F can match the stress fields for two-component turbulence and axisymmetric turbulence quite good for the present simulation data. Expressions (5.14) and (5.15) are identical to the model derived in [13]. In equation (5.13) for ψ_{2C} a modification factor $[0.02 + 0.03\exp(-Re_t)]$ fitted from the present DNS data is added here to take account of the influence of the turbulence Reynolds number.

The approximate form of T_s (Eq. 5.11) is tested by using the DNS data for Rayleigh-Bénard convection. The data presented by circles in Fig. 5.5 are evaluated from the numerical simulation, where fourth order derivatives are required (see [12]). In general, the results in Fig. 5.5 show a good agreement between the evaluated and the predicted data. In the near wall region, where large gradients of the statistical quantities exist, the spatial discretisation is not fine enough to calculate the high order derivatives with high accuracy. Therefore, close to the wall in Fig. 5.5 the data scatter. In general, the comparison of the model for the sink term T_s with the exact sink term evaluated from the DNS data shows a good agreement for Rayleigh-Bénard convection in both, air and sodium.

5.3 Model for the buoyant production term

Let us now consider the second term in the dynamic equation (5.1) for ϵ_h which needs closure, i.e the term

$$T_b = \nu\beta g_s[(\Delta_\xi\overline{\theta u_s'})_0 + (\Delta_\xi\overline{u_s\theta'})_0] \tag{5.20}$$

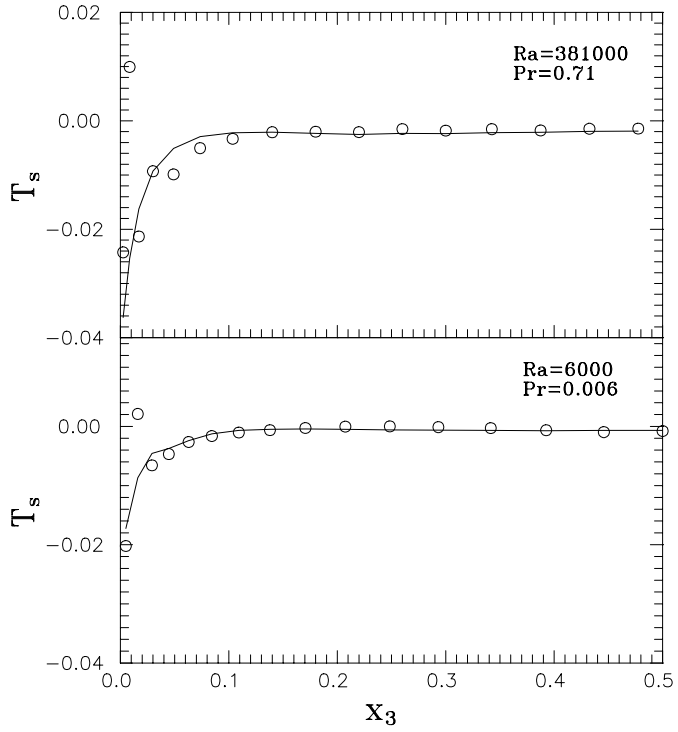

Figure 5.5: Distribution of sink term T_s. ——, Eq. (5.11); ∘, value evaluated from DNS data ($T_s = T1 + T3$, see Fig. 4.3(b)).

This term contributes to the buoyant production $P_{\epsilon b}$, which is in equation (4.5) decomposed in

$$P_{\epsilon b} = -2\nu\beta g_i \overline{\frac{\partial\theta}{\partial x_l}\frac{\partial u_i}{\partial x_l}} = -\frac{1}{2}\nu\beta g_i \Delta_x \overline{\theta u_i} + T_b. \tag{5.21}$$

As shown in section 4.2, the two-point temperature-velocity-correlations are not locally homogeneous and therefore the term T_b is not zero and needs modelling. Due to Eq. (5.21), in second order modelling of the turbulent heat fluxes the formulation of an accurate model for T_b represents at the same time a closure for the buoyant production $P_{\epsilon b}$.

Theoretically, a dynamic equation for $(\Delta_\xi \overline{u_i\theta'})_0$ or $(\Delta_\xi \overline{\theta u_i'})_0$ and thus for T_b can be derived by using the two-point correlation technique, as it was done for $(\Delta_\xi \overline{u_i u_j'})_0$. However, such an equation will be difficult to simplify, since, according to the study in section 4, the assumption of local homogeneity can not be used for the temperature field, at least for the present turbulence Peclet numbers. Hence, another approach is needed to develop a model for the buoyant production T_b in the dissipation equation.

For the closure of T_b it is assumed that the derivatives with respect to ξ can be expressed in terms of a single-point second order correlation $\overline{\theta u_s}$. Using the scaling analysis proposed

by Tennekes & Lumley [24] the buoyant production in Eq. (5.1) can be approximated by

$$T_b = \nu\beta g_s[(\Delta_\xi \overline{\theta u_s'})_0 + (\Delta_\xi \overline{u_s \theta'})_0] \simeq C_{\epsilon 3}\frac{\epsilon_h}{k}G, \tag{5.22}$$

where

$$G = -\beta g_s \overline{u_s \theta} \tag{5.23}$$

is the buoyant production term in the k-equation. In the literature, the coefficient $C_{\epsilon 3}$ is usually adopted as a constant or it is corrected, depending whether the buoyant shear layer is horizontal or vertical [21]. An influence of the fluid Prandtl number is not taken into account. This is, however, a major drawback, as can be argued by considering the dissipation term $\epsilon_{i\theta}$ in the transport equation for the turbulent heat flux $\overline{u_i\theta}$,

$$\epsilon_{i\theta} = (\nu + \alpha)\overline{\frac{\partial u_i}{\partial x_l}\frac{\partial \theta}{\partial x_l}}. \tag{5.24}$$

Comparing the definitions of $\epsilon_{i\theta}$ and $P_{\epsilon b}$ it appears, that both terms involve the same correlation of derivatives, namely $\overline{\frac{\partial u_i}{\partial x_l}\frac{\partial \theta}{\partial x_l}}$.

In the appendix the analytical transport equation for $\epsilon_{i\theta}$ is given. From this equation it can be concluded that $\epsilon_{i\theta}$ is clearly influenced by the Prandtl number. In practice, more sophisticated models for $\epsilon_{i\theta}$ already account for the effect of the fluid Prandtl number (see e.g. the model of Shikazono & Kasagi [23]) . Thus, it is appropriate to consider $C_{\epsilon 3}$ as function of Prandtl number. In addition, similar to the model in [23] for $\epsilon_{i\theta}$, in the model for $P_{\epsilon b}$ to be developed $C_{\epsilon 3}$ shall be a function of the ratio of turbulent thermal and mechanical time scale R, defined as

$$R = \frac{\tau_\theta}{\tau} = \frac{\overline{\theta^2}}{2\epsilon_\theta}\frac{\epsilon}{k}. \tag{5.25}$$

Here, ϵ_θ is the thermal dissipation rate

$$\epsilon_\theta = \alpha\overline{\frac{\partial \theta}{\partial x_l}\frac{\partial \theta}{\partial x_l}} \tag{5.26}$$

Using DNS data for Rayleigh-Bénard convection in different fluids for different Rayleigh numbers, Wörner & Grötzbach [6, 27, 28] analysed the effect of Prandtl number and turbulence level on the turbulence time scale ratio R. In Figure 5.6 profiles of R are given only for the simulations relevant to the present study. At the walls, for isothermal wall condition R just takes the value of Pr. For air, the overall value of R is about 0.85, which is the value usually adopted in turbulence modelling. However, Figure 5.6 shows that it is not appropriate if a constant value of R is used for $Pr \neq 1$. For $Pr \ll 1$ the temperature boundary layer is quite thicker than the velocity boundary layer, and the time scale τ_θ for the temperature fluctuations is smaller than τ for the velocity fluctuations. Therefore the time scale ratio R decreases with decreasing Prandtl number.

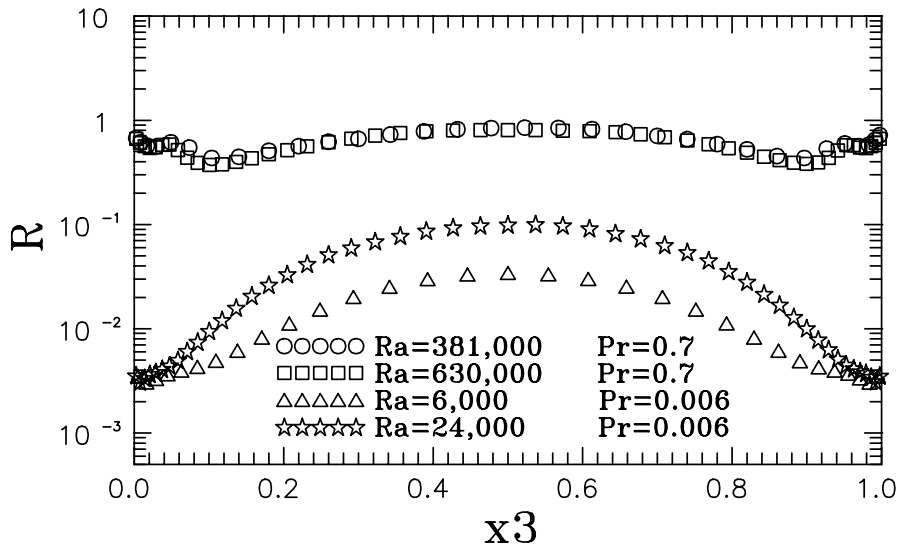

Figure 5.6: Distribution of R. $\circ$, $Ra = 381,000$, $Pr = 0.71$; $\square$, $Ra = 630,000$, $Pr = 0.71$; $\triangle$, $Ra = 6,000$, $Pr = 0.006$; $\star$, $Ra = 24,000$, $Pr = 0.006$.

With increasing turbulence level the thickness of the temperature boundary layer will be reduced, which results in an increase of the time scale ratio R.

In order to obtain R in the application of such models, the extra information about the thermal dissipation rate ϵ_θ of the temperature variance $\overline{\theta^2}$ is required. This information is obtained by solving a transport equation for ϵ_θ. This implies, however, an additional computational expense. It can be avoided by introducing the heat flux anisotropy invariant

$$A_\theta = \frac{\overline{u_i\theta} \cdot \overline{u_i\theta}}{\overline{u_j u_j} \cdot \overline{\theta^2}} \tag{5.27}$$

instead of R. The parameter A_θ was used e.g. by Haroutunian & Launder [9] to model $\overline{u_i\theta}$ for free buoyant shear flows. However, it is difficult to find appropriate general functions in terms of A_θ, which can account for the wall effects in the models for $P_{\epsilon b}$ or $\overline{u_i\theta}$. In the present approach, therefore the time scale ratio R is used instead of A_θ.

The new model proposed here for the buoyant production T_b in Eq. (5.1) reads:

$$T_b = \nu\beta g_s[(\Delta_\xi \overline{\theta u_s'})_0 + (\Delta_\xi \overline{u_s \theta'})_0] \simeq \left(\frac{Pr}{R}\right)^{0.7} \frac{\epsilon_h}{k} G. \tag{5.28}$$

Herein, the term $(Pr/R)^{0.7}$ is obtained by fitting the DNS data for Rayleigh-Bénard convection. A comparison between the model results from Eq. (5.28) and the results evaluated from the DNS data is shown in Figure 5.7. The proposed form for T_b agrees

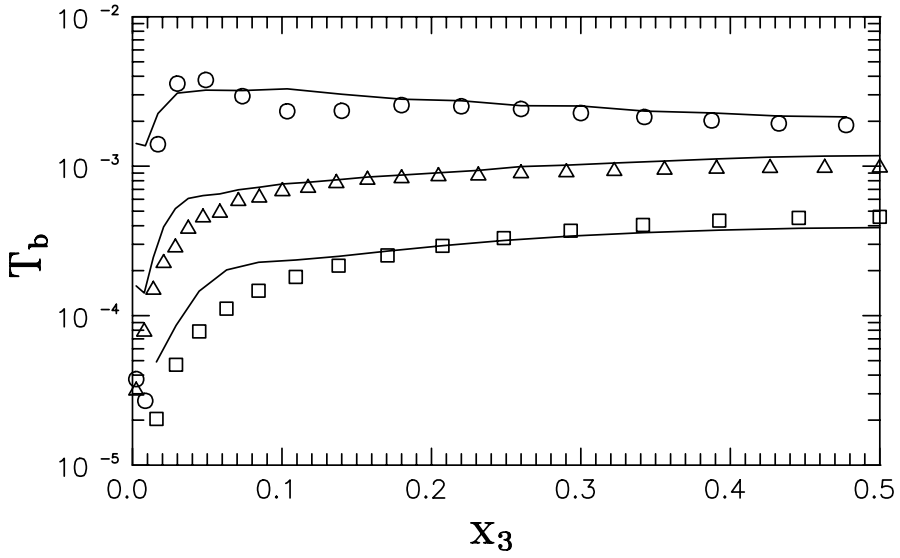

Figure 5.7: Distribution of buoyant production term T_b. ——, model of Eq. (5.28); $\circ$, DNS data $Ra = 381,000$, $Pr = 0.71$; $\triangle$, $Ra = 24,000$, $Pr = 0.006$; $\square$, $Ra = 6,000$, $Pr = 0.006$.

well with the DNS data except for a few points in the region near the wall. In total, the new model for $P_{\epsilon b}$ is expressed as follows:

$$P_{\epsilon b} \simeq -\frac{1}{2}\nu\beta g_i \Delta_x \overline{\theta u_i} + \left(\frac{Pr}{R}\right)^{0.7} \frac{\epsilon_h}{k} G. \tag{5.29}$$

In the following, we compare the new model for the buoyant production in the dissipation equation with models already available in literature. Rodi [21] introduced a flux Richardson number to account for the influence of the direction of the buoyant shear layer on the production term in the ϵ equation. For a horizontal channel the corresponding buoyancy production term can be written as:

$$P_{\epsilon b} = -2\nu\beta g_i \overline{\frac{\partial\theta}{\partial x_l}\frac{\partial u_i}{\partial x_l}} \simeq \frac{1}{5} C_{\epsilon 1} \frac{\epsilon}{k} G, \tag{5.30}$$

and for a vertical channel:

$$P_{\epsilon b} = -2\nu\beta g_i \overline{\frac{\partial\theta}{\partial x_l}\frac{\partial u_i}{\partial x_l}} \simeq C_{\epsilon 1} \frac{\epsilon}{k} G, \tag{5.31}$$

where $C_{\epsilon 1} = 1.44$. Conventionally, the coefficient $C_{\epsilon 1}$ is the same as is used in the model for the production term by the mean velocity field

$$P_\epsilon^1 = -C_{\epsilon 1} \frac{\epsilon \overline{u_k u_s}}{k} \frac{\partial U_s}{\partial x_k}. \tag{5.32}$$

According to Rodi, in the horizontal case $P_{\epsilon b}$ is only one fifth of that one in the vertical channel. Ince & Launder [11], however, preferred the following form

$$P_{\epsilon b} = -2\nu\beta g_i \overline{\frac{\partial\theta}{\partial x_l}\frac{\partial u_i}{\partial x_l}} \simeq C_{\epsilon 1}\frac{\epsilon}{k}G \tag{5.33}$$

rather than Eq. (5.30).

The profiles predicted for $P_{\epsilon b}$ by models (5.30), (5.33), and (5.29) are compared with the analytical term $P_{\epsilon b}$ computed directly from the Rayleigh-Bénard DNS data for air ($Ra = 381,000$) in Figure 5.8 and for sodium ($Ra = 24,000$) in Figure 5.9. For air, Rodi's model underestimates $P_{\epsilon b}$ strongly, but Ince & Launder's model overestimates $P_{\epsilon b}$ in the center of the channel, see Fig. 5.8. For liquid sodium, both models give too high values in the channel center and too low values in the near wall region, see Fig. 5.9. However, the data calculated from the present model, Eq. (5.29), agree overall very well with the DNS data.

For the internally heated natural convection, the present model results in an overestimation of $P_{\epsilon b}$ while the models of Rodi and Launder result in an underprediction, see Figure 5.10. However, in this case the overall maximum turbulence Reynolds number is only about four. Besides this quantitative disagreement, there is also a qualitative disagreement. While in the range $0.1 < x_3 < 0.2$ the DNS data show a small but positive $P_{\epsilon b}$, all models predict negative values in this range. This failure is caused by the fact that in all models the buoyant production is directly proportional to the turbulent heat flux. In the range $0.1 < x_3 < 0.2$, however, the turbulent heat flux is negative, see [22, 30]. Therefore, negative values of $P_{\epsilon b}$ are predicted by the models, which means that buoyancy does not act to produce dissipation but to destroy it. Obviously, as the DNS data show, this is unrealistic and the models need to be improved to account for this phenomenon.

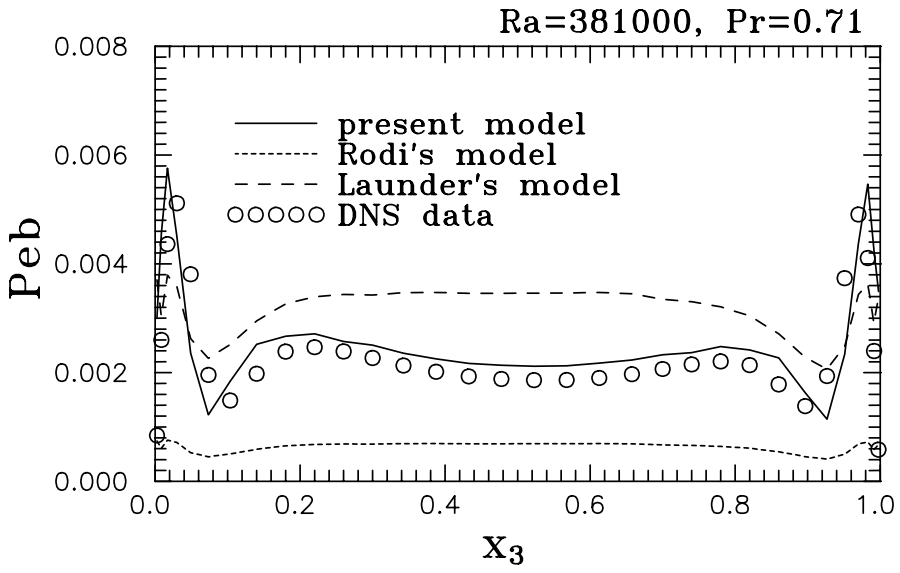

Figure 5.8: Comparison of models for $P_{\epsilon b}$. Rayleigh-Bénard convection in air ($Ra = 381,000$, $Pr = 0.71$). ---, Eq. (5.30); ———, Eq. (5.33); ——, Eq. (5.29); ∘, DNS data.

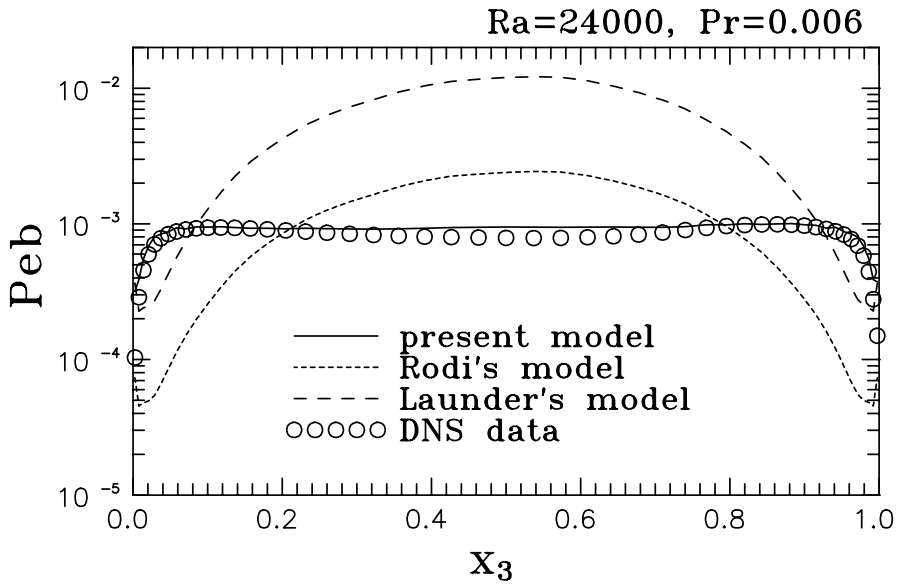

Figure 5.9: Comparison of models for $P_{\epsilon b}$. Rayleigh-Bénard convection in sodium ($Ra = 24,000$, $Pr = 0.006$). ---, Eq. (5.30); ———, Eq. (5.33); ——, Eq. (5.29); ∘, DNS data.

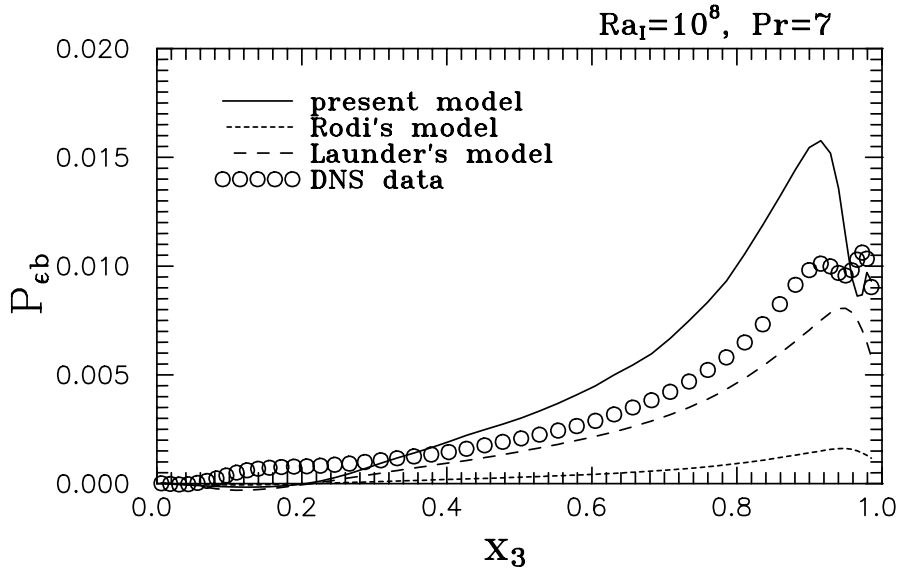

Figure 5.10: Comparison of models for $P_{\epsilon b}$. Internally heated convection ($Ra_I = 10^8$, $Pr = 7$). ---, Eq. (5.30); — — —, Eq. (5.33); ——, Eq. (5.29); ∘, DNS data.

5.4 Budget of the modelled equation for ϵ_h

With the models developed in section 5.2 and 5.3, the closed equation for the homogeneous part of the dissipation rate takes the form:

$$\frac{\partial \epsilon_h}{\partial t} \simeq \left(\frac{Pr}{R}\right)^{0.7} \frac{\epsilon_h}{k} G - \psi \frac{\epsilon_h^2}{k} + \frac{1}{2} \nu \Delta_x \epsilon_h. \tag{5.34}$$

An examination of the model quality can be performed by computing the budget of the closed equation using the DNS data. Here, this is done for Rayleigh-Bénard convection in air at $Ra = 381,000$. For fully developed convection, the rate of change term on the left-hand side of Eq. (5.34) is zero. Therefore, the sum of all terms on the right-hand side should be zero, too. Figure 5.11 presents the distribution of these terms as well as their budget, computed by summing up all terms. It can be seen that the buoyant production term T_b is positive in the channel center, where it almost balances the sink term. Close to the wall, where T_b is small, the sink term is balanced by the viscous diffusion (last term on r.h.s of Eq. (5.34)), which takes high positive values inside the viscous boundary layer. While the imbalance in the near-wall region is somewhat large, Figure 5.11 in general shows only a small imbalance across the channel.

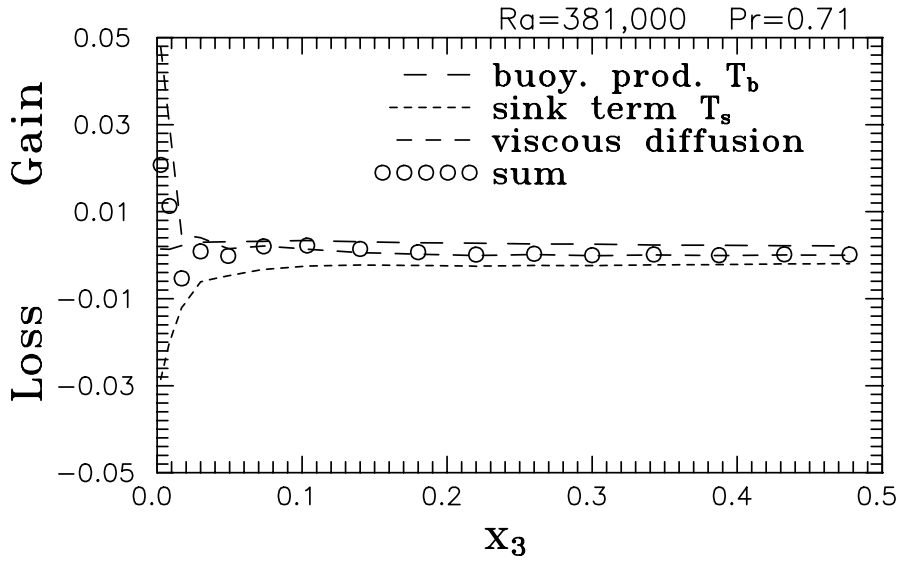

Figure 5.11: Terms in the budget Eq. (5.34) deduced from the DNS data ($Ra = 381,000$, $Pr = 0.71$). ---, T_s calculated from Eq.(5.11); −−−, $1/2\nu\Delta_x\epsilon_h$; ———, T_b calculated from Eq. (5.28); ∘, sum of all terms.

5.5 Components of the dissipation tensor

For full second order turbulence modelling, the components of the dissipation tensor are required. Based on the two-point correlation technique and invariant theory, the following partition of the dissipation tensor was proposed in [13, 32]:

$$\epsilon_{ij} = \frac{1}{4}\nu\Delta_x\overline{u_iu_j} + (\epsilon - \frac{1}{2}\nu\Delta_x k)\left\{\frac{1}{3}(1-A)\delta_{ij} + A\frac{\overline{u_iu_j}}{2k}\right\}, \tag{5.35}$$

$$\epsilon = \frac{1}{4}\nu\Delta_x\overline{u_su_s} + \epsilon_h, \tag{5.36}$$

$$A = (1-F) + 9[\frac{3}{4}(\frac{4}{3}|III|)^{2/3} - III]F. \tag{5.37}$$

Eq. (5.35) represents a linear relation between the anisotropy tensor of the dissipation and the anisotropy tensor of the Reynolds stress. The invariant function A (see [32] for the detailed derivation) is also the model coefficient for the non-buoyant production term in the ϵ_h-equation, which was not considered here because in Rayleigh-Bénard convection it is zero. In Figure 5.12, results are presented for $\epsilon_{11}, \epsilon_{22}$ and ϵ_{33} calculated from model (5.35) by using the DNS data for ϵ_h and $\overline{u_iu_j}$ of Rayleigh-Bénard convection in air (note that here $\epsilon_{ij} = 0$, if $i \neq j$). While for ϵ_{11} and ϵ_{22} a very good agreement between the results from Eq. (5.35) and the values for $\epsilon_{11}, \epsilon_{22}$ evaluated directly from the DNS data is obtained, the model performance for ϵ_{33} is not fully satisfactory.

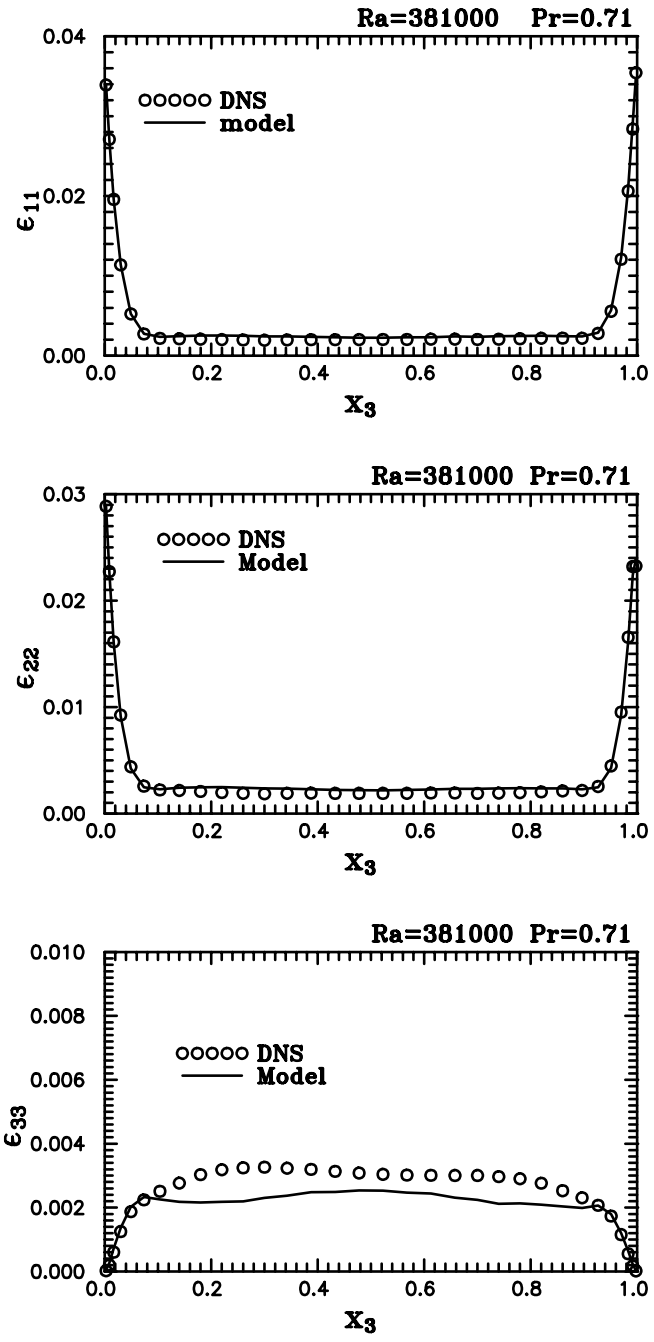

Figure 5.12: Distribution of the diagonal components of the dissipation tensor. Rayleigh-Bénard convection in air, $Ra = 381,000$. $\circ$, DNS data; ——, equation (5.35).

6 Modelling of the heat flux dissipation term $\epsilon_{i\theta}$

The dissipation term $\epsilon_{i\theta}$ is one of the unknown terms in the transport equations for the heat fluxes $\overline{u_i\theta}$ (see Eq. (1.2)). For isotropic turbulence $\epsilon_{i\theta}$ is zero. In this case, the so called pressure-scrambling term is the only sink term in the $\overline{u_i\theta}$-equation. However, in buoyant flows which always are more or less non-isotropic $\epsilon_{i\theta}$ can be an important sink term. Kawamura & Ohsaka [14], for example, perform direct numerical simulations of turbulent heat transfer in channel flow for various Prandtl numbers ranging from 0.025 to 5. They find that the dominant sink term in the turbulent heat flux equation is the pressure-scrambling term in case of $Pr > 0.2$, while for smaller Prandtl numbers $\epsilon_{i\theta}$ is overwhelming. For Rayleigh-Bénard convection in liquid sodium at $Ra = 24,000$ DNS data show that $\epsilon_{i\theta}$ is the dominant sink term, and that it far exeeds the pressure-scrambling term [28]. Thus, appropriate modelling of $\epsilon_{i\theta}$ is very important for buoyant flows, especially at low Prandtl or Peclet numbers.

6.1 Interpretation of $\epsilon_{i\theta}$ by the two-point correlation technique

In correspondence to the statistical interpretation of the dissipation correlations in the equations of second-order moments $\overline{u_iu_j}$, the dissipation correlations in the equations of the turbulent heat fluxes $\overline{u_i\theta}$ can also be expressed as sum of an inhomogeneous and a homogeneous part:

$$\begin{aligned}\epsilon_{i\theta} &= (\nu+\alpha)\overline{\frac{\partial\theta}{\partial x_l}\frac{\partial u_i}{\partial x_l}} \\ &= \underbrace{\frac{1}{4}(\nu+\alpha)\Delta_x\overline{\theta u_i}}_{\text{inhomogeneous}} \underbrace{-\frac{1}{2}(\nu+\alpha)[(\Delta_\xi\overline{\theta u_i'})_0 + (\Delta_\xi\overline{u_i\theta'})_0]}_{\text{homogeneous}}\,. \end{aligned} \tag{6.1}$$

In turbulent Rayleigh-Bénard convection the turbulent heat fluxes in the horizontal directions are zero and only $\overline{u_3\theta}$ exists. Therefore, in the following only $\epsilon_{3\theta}$ is investigated. Figures 6.1 - 6.3 display the distribution of the inhomogeneous and homogeneous part of $\epsilon_{3\theta}$ for Rayleigh-Bénard convection in air ($Ra = 381,000$) and sodium ($Ra = 6,000$ and $Ra = 24,000$). The values of $\epsilon_{3\theta}$ go to zero at the wall, which can be also obtained by expanding the instantaneous quantities in a Taylor series near the wall. Far away from the wall the inhomogeneous part of $\epsilon_{3\theta}$ can be expected to tend to zero for high turbulence Peclet numbers. However, for low turbulence Peclet numbers it does not vanish even in the center of the channel, see Figs. 6.2 and 6.3. This behaviour is quite different from that of the inhomogeneous part of the dissipation of turbulence kinetic energy, compare with Figs. 3.3 - 3.5.

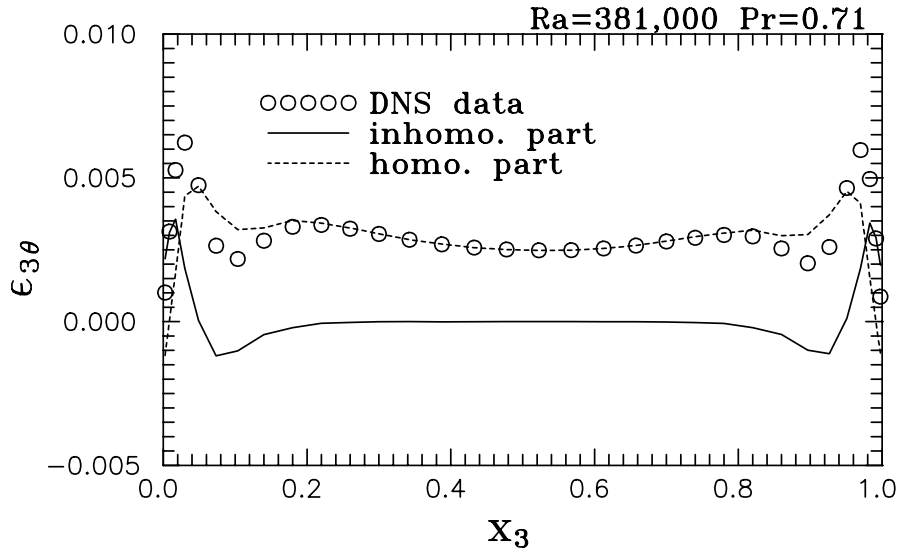

Figure 6.1: Distribution of $\epsilon_{3\theta}$. DNS data of Rayleigh-Bénard convection in air ($Ra = 381,000$), $Pe_t = 76$.

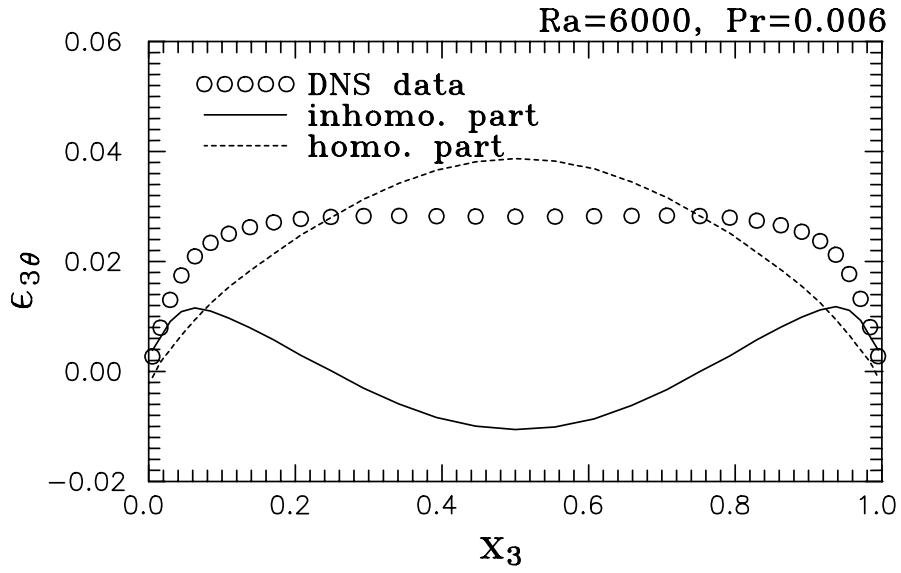

Figure 6.2: Distribution of $\epsilon_{3\theta}$. DNS data of Rayleigh-Bénard convection in sodium ($Ra = 6,000$), $Pe_t = 3$.

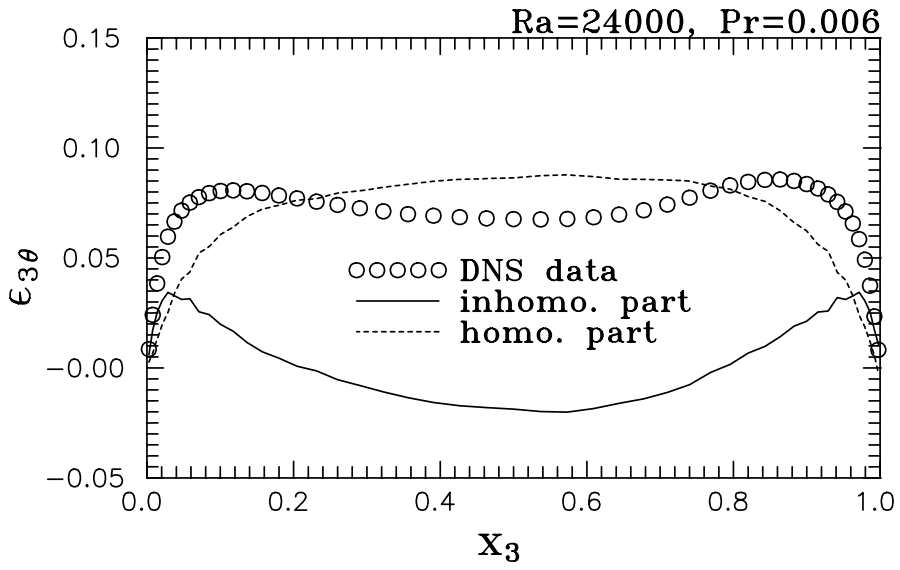

Figure 6.3: Distribution of $\epsilon_{3\theta}$. DNS data of Rayleigh-Bénard convection in sodium ($Ra = 24,000$), $Pe_t = 13$.

6.2 Model for $\epsilon_{i\theta}$

In the previous section the dissipation term $\epsilon_{i\theta}$ was decomposed into two parts. The inhomogeneous part is related to $\overline{u_i\theta}$ which is known by second-order moment closure. Therefore, only the homogeneous part which is expressed as a function of two-point correlations must be modeled. A corresponding dynamic equation, like the equation for ϵ_h, can be derived theoretically. However, this equation is more complicated than that for ϵ_h and can hardly be simplified.

In fact, a model for $\epsilon_{3\theta}$ can be obtained by using results of section 5.3. Comparing the definition of $P_{\epsilon b}$ and $\epsilon_{i\theta}$, one notices that both terms contain the same correlation $\overline{\frac{\partial\theta}{\partial x_l}\frac{\partial u_i}{\partial x_l}}$. Hence, $\epsilon_{i\theta}$ should be modelled consistent to $P_{\epsilon b}$ by using an equivalent closure assumption. Since the homogeneous part of the above correlation was obtained, the model for $\epsilon_{i\theta}$ can be easily expressed as:

$$\epsilon_{i\theta} \simeq \frac{1}{4}(\nu+\alpha)\Delta_x\overline{\theta u_i} + \frac{1}{2}(1+\frac{1}{Pr})\left(\frac{Pr}{R}\right)^{0.7}\frac{\epsilon_h}{k}\overline{u_i\theta}. \tag{6.2}$$

The dissipation term $\epsilon_{3\theta}$ is calculated via Eq. (6.2) and is compared in Fig. 6.4 with the value of $\epsilon_{3\theta}$ computed directly from the DNS data. As can be seen, a very good agreement is achieved by model (6.2) for different fluids (i.e. Prandtl numbers) and different turbulence levels.

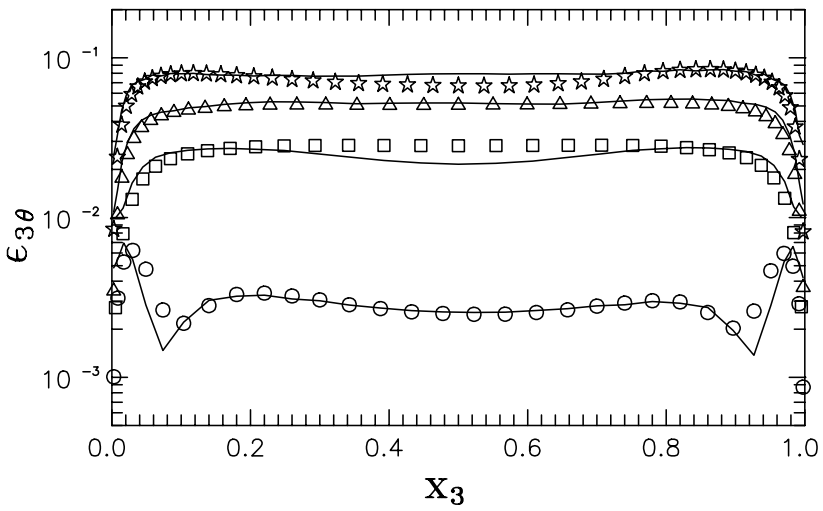

Figure 6.4: Distribution of $\epsilon_{3\theta}$. —— Eq. (6.2), DNS data: $Pr = 0.006$: $\star$ $Ra = 24,000$; $\triangle$ $Ra = 12,000$; $\square$ $Ra = 6,000$; $\circ$ $Pr = 0.71$, $Ra = 381,000$.

6.3 Comparison with models from literature

In this paragraph we compare the new model for $\epsilon_{i\theta}$ with models available in literature. Based on isotropic and homogeneous shear turbulence, Shikazono & Kasagi [23] developed a model for $\epsilon_{i\theta}$ which incorporates the effect of the Prandtl number. The model was also modified to be applicable to wall turbulence:

$$
\begin{aligned}
\epsilon_{i\theta} &= \left\{ \frac{1+Pr}{2Pr}\frac{\epsilon}{k}\overline{u_i\theta} + \frac{1+Pr}{2Pr}\frac{\epsilon}{k}\overline{u_k\theta}n_i n_k \right\} f_w \\
&\quad + \left\{ C_\epsilon f_{\epsilon 1} f_{\epsilon 2} f_{\epsilon w} \frac{1+Pr}{2\sqrt{Pr}\sqrt{R}}\frac{\epsilon}{k}\overline{u_i\theta} \right\}(1-f_w), \\
&\quad f_w = \exp[-C_{w1}\sqrt{J}], \quad C_{w1} = max[4, 0.6Pr^{3/4}], \\
&\quad f_{\epsilon 1} = 1-\exp(-10r), \quad r = \frac{C_R/R+1}{\sqrt{Re_t} f_{II2}}, \\
&\quad f_{II2} = min\left[1, \frac{1}{1.2}\frac{\sqrt{Pr}}{\sqrt{R}}\right], \quad f_{\epsilon 2} = min\left[6\frac{\sqrt{Pr}}{\sqrt{R}}, 1, \frac{\sqrt{R}}{\sqrt{Pr}}\right], \\
&\quad f_{\epsilon w} = min\left[1, \frac{C_R}{R} + C_s\sqrt{Re_t}\right].
\end{aligned} \tag{6.3}
$$

Here, n_i is the wall normal unit vector. The coefficients take the values $C_R = 0.7$ and $C_s = 0.1$. J is the invariant function defined by Eq. (5.18) and f_w changes from unity (at the wall) to zero (far away from the wall). The functions f_w and $f_{\epsilon w}$ account for wall effects.

Wörner & Grötzbach [29] proposed the following model for pure natural convection which is, however, valid only far away from the wall:

$$\epsilon_{i\theta} = \exp(-0.0007(Re_t + Pe_t))\frac{1+Pr}{2\sqrt{Pr}\sqrt{R}}\frac{\epsilon}{k}\overline{u_i\theta}. \tag{6.4}$$

The factor $\exp(-0.0007(Re_t + Pe_t))$ was used to account for the molecular effects and the value 0.0007 was fitted against DNS data of Rayleigh-Bénard convection at various Prandtl and Rayleigh numbers.

For Rayleigh-Bénard convection in air, the profiles for $\epsilon_{3\theta}$ predicted by the three models according to Eq. (6.3), Eq. (6.4), and Eq. (6.2), are shown in Figure 6.5. All models give similar results in the center of the channel. However, in the near wall region the new model, Eq. (6.2), gives the best performance.

In Figure 6.6(a-c) the results for Rayleigh-Bénard convection in sodium are given. The model of Shikazono & Kasagi, Eq. (6.3), strongly overestimates $\epsilon_{3\theta}$ in the channel center. It seems that Eq. (6.3) is not suitable for pure natural convection, especially for flows with quite small Prandtl numbers. The model of Wörner & Grötzbach, Eq. (6.4), agrees well with the sodium DNS data for $Ra = 6,000$ and $Ra = 12,000$ in the center of the channel but gives too low values for $Ra = 24,000$, see Fig. 6.6(c). In the wall and buffer regions both models, Eq. (6.3) and Eq. (6.4), can not predict correct values of $\epsilon_{3\theta}$. This ist not surprising for the model of Wörner & Grötzbach which does not involve any wall correction. While, on the other hand, the model of Shikazono & Kasagi contains a wall correction formulated for forced convection, the present results show that it is not appropriate for pure natural convection flows. For sodium at very small Peclet numbers the present model, Eq. (6.2), underestimates $\epsilon_{i\theta}$ a little in the center of the channel, see Figure 6.6(a) for $Ra = 6,000$. A further modification in the model for the homogeneous part of $\epsilon_{i\theta}$ should therefore be introduced in the future, in order to incorporate the influence of the Peclet number.

From experience in turbulence modelling it is well known that the flow in the wall region, where strong anisotropy appears, is usually difficult to be treated. Invariant functions are used more and more to construct wall correction factors, e.g. f_w in Eq. (6.3), and for closure of the sink term of the dissipation rate discussed in section 5. However, it might not be appropriate to use the invariant functions of the velocity field also in the temperature field. The decomposition of $\epsilon_{i\theta}$ based on the two-point correlation technique (see Eq. 6.1) results in an inhomogeneous part of $\epsilon_{i\theta}$ which accounts perfectly for the wall effect, as it is seen in Fig. 6.5 and Fig. 6.6.

For internally heated natural convection, where the turbulence Reynolds number is very small, the new model overestimates $\epsilon_{3\theta}$, see Figure 6.7. Model (6.4) gives a good prediction in the range $0.2 < x_3 < 0.8$. For $x_3 \leq 0.2$ all three models fail to predict correct values of $\epsilon_{i\theta}$. The negative values of $\overline{u_i\theta}$ in this range result in the negative values of $\epsilon_{i\theta}$ which are physically not correct, compare with the DNS data in Fig. 6.7.

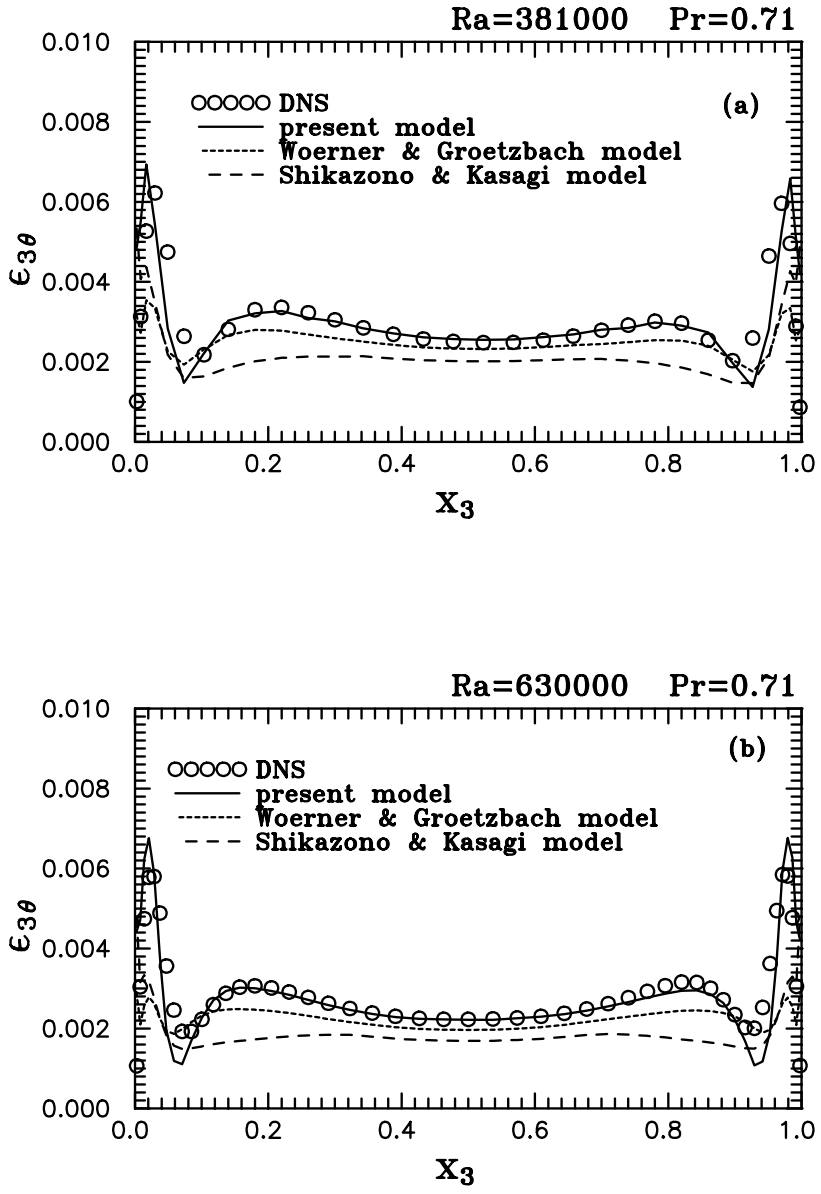

Figure 6.5: $\epsilon_{3\theta}$ for Rayleigh-Bénard convection in air ($Pr = 0.71$). (a): $Ra = 381,000$, (b): $Ra = 630,000$. —— Eq. (6.2), ----; Eq. (6.4), – – –; Eq. (6.3), ∘; DNS data.

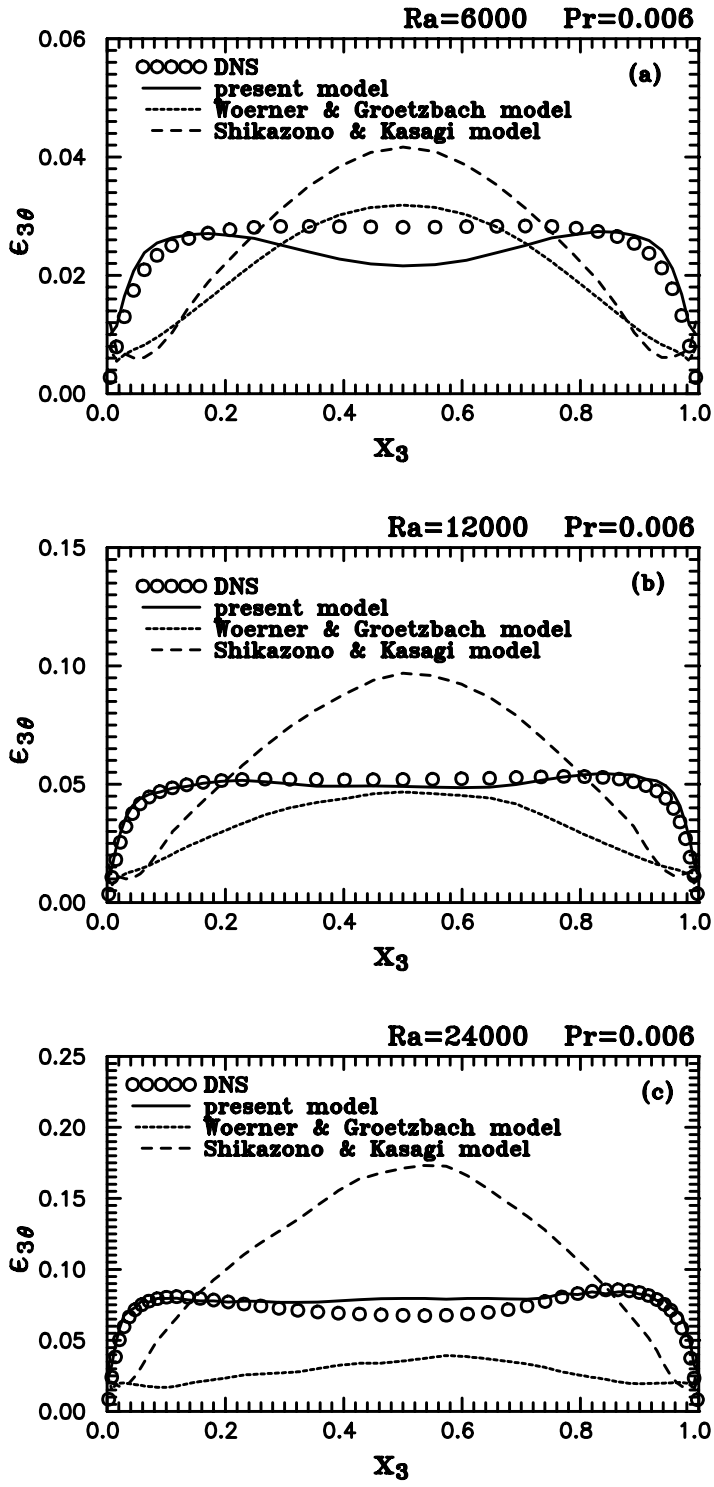

Figure 6.6: $\epsilon_{3\theta}$ for Rayleigh-Bénard convection in sodium ($Pr = 0.006$). (a): $Ra = 6,000$, (b): $Ra = 12,000$, (c): $Ra = 24000$. —— Eq. (6.2), ----; Eq. (6.4), −−−; Eq. (6.3), ∘; DNS data.

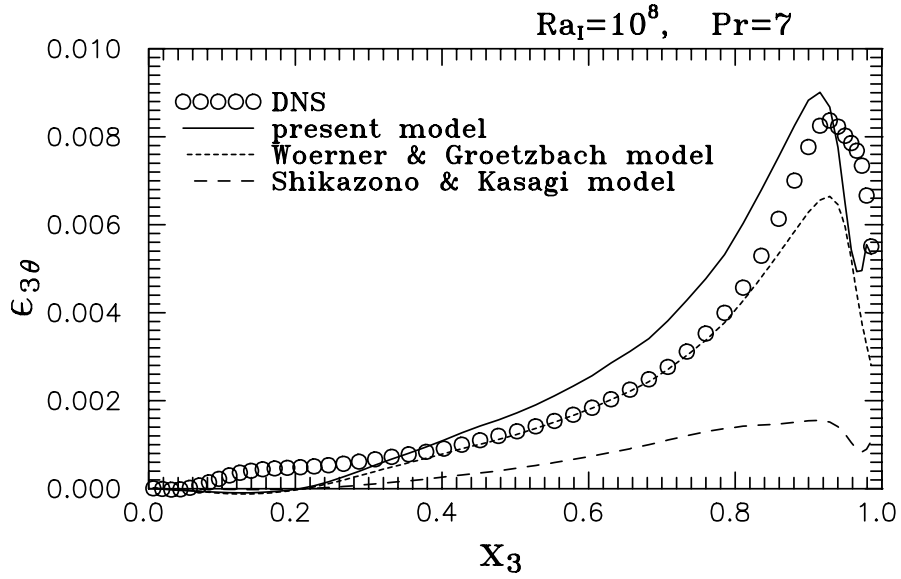

Figure 6.7: Distribution of $\epsilon_{3\theta}$ for internally heated convection ($Pr = 7, Ra_I = 10^8$). $\circ$; DNS data, ——; Eq. (6.2), ----; Eq. (6.4), – – –; Eq. (6.3).

7 Conclusions

In this report the closure of the equation for the turbulent dissipation rate, which was developed earlier based on the two-point correlation technique and invariant theory for shear turbulence, is investigated by means of direct numerical simulation (DNS) data of turbulent Rayleigh-Bénard convection in air and sodium and of internally heated natural convection.

The validity of the assumption of local homogeneity for the small scale turbulence, which is used to simplify the analytically derived equation for the turbulent dissipation rate, is tested for Rayleigh-Bénard convection. It is shown that for the derivatives of two-point velocity correlations of third rank the assumption can be used, but not for the derivatives of the two-point velocity-temperature correlation of second rank.

The DNS data for Rayleigh-Bénard convection and internally heated natural convection are plotted in the anisotropic invariant map (AIM). It is found that the anisotropy of the Reynolds stresses for turbulent natural convection is weaker than that for wall bounded turbulent shear flow. A clear turbulence Reynolds number effect can be seen from the results in the anisotropic invariant map. Based on the AIM, a model is developed for the sink term in the dynamic equation for the homogeneous dissipation rate. The model results are in good agreement with the DNS data.

For turbulent natural convection, the buoyant production term in the dissipation rate equation is also of importance. Up to now, the model for the buoyant production term $P_{\epsilon b}$ in the ϵ-equation and the model for the dissipation term $\epsilon_{i\theta}$ in the $\overline{u_i\theta}$-equation were always developed in different ways, though both closure terms involve the same correlation. A new consistent model for both, $P_{\epsilon b}$ and $\epsilon_{i\theta}$ is developed, where the Prandtl number and the turbulence time scale ratio R are the main parameters. The new models proposed provide accurate predictions for fully developed Rayleigh-Bénard convection in air and sodium and do properly account for the influence of the Prandtl number and the turbulence level, as well as for wall effects. As compared with other models in literature, the new model is relatively simple and does not involve any complicated wall correction formulations. The models developed for $P_{\epsilon b}$ and $\epsilon_{i\theta}$ can be easily put into use in CFD computer codes, e.g. in the FLUTAN code, to improve the turbulence modelling features for strongly buoyant flows.

For further investigations, the models developed should be tested or improved by using further DNS data of different types of turbulent natural convection, e.g. internally heated convection with different Rayleigh numbers. For the DNS data of the internally heated convection investigated in the present study ($Ra_I = 10^8$), the turbulence Reynolds number is quite low ($Re_t \simeq 4$). These DNS data might be useful for studying low-Reynolds number effects, however, it is a matter of opinion whether it is meaningful to constrain the model by such small Reynolds numbers, since in practical applications the turbulence Reynolds number is much higher.

References

[1] Antonia, R.A., Kim, J. & Browne, L.W.B. 1991 Some characteristics of small-scale turbulence in a turbulent duct flow. *J. Fluid Mech.*, 233:369–388.

[2] Chou, P.Y. 1945 On the velocity correlation and the solution of equation of turbulent fluctuation. *Quart. Appl. Math.*, 3:38–54.

[3] Carteciano, L.N. 1996 Entwicklung eines Turbulenzmodells für Auftriebsströmungen. PhD thesis, Universität Karlsruhe (TH), FZKA 5775.

[4] Coleman, G.N. & Mansour, N.N. 1991 Simulation and modelling of homogeneous compressible turbulence under isotropic mean compression. In *Proc. Eight Symp. on Turbulent Shear Flows*, Munich, pages 21.3.1-21.3.6.

[5] Grötzbach, G. 1987 Direct numerical and large eddy simulation of turbulent channel flow. *Encyclopedia of Fluid Mechanics*, 6:1337–1391.

[6] Grötzbach, G. & Wörner, M. 1992 Analysis of second order transport equations by numerical simulations of turbulent convection in liquid metals. In *Proc. NURETH-5*, Salt Lake City, USA, Vol. 2, pp. 358–365.

[7] Grötzbach, G. & Wörner, M. 1993 Analysis of flow mechanisms in Rayleigh-Bénard convection at small Prandtl number. In *Proc. Joint Int. Conf. on Mathematical Methods and Supercomputing in Nuclear Applications*, Karlsruhe, Germany, Vol. 1, pp. 236–247.

[8] Hanjalić, K. 1994 Achievements and limitations in modelling and computation of buoyant turbulent flows and heat transfer. In *Proc. 10th Int. Heat Transfer Conf.*, Volume 1, pp. 1–18, Brighton, U.K.

[9] Haroutunian, V. & Launder, B.E. 1988 Second-moment modelling of free buoyant shear flows: a comparison of parabolic and elliptic solutions. In *Stably Stratified Flow and Dense Gas Dispersion*, Ed.: Puttock, pp. 409–430, Oxford.

[10] Hinze, J.O., 1975 *Turbulence*. Mc Graw-Hill Book Company, 2nd ed.

[11] Ince, N.Z. & Launder, B.E. 1989 On the computation of buoyance-driven turbulent flows in rectangular enclosures. *Int. J. Heat and Fluid Flow*, 10:110–117.

[12] Jovanović, J., Ye, Q.-Y. & Durst, F. 1995 Statistical interpretation of the turbulent dissipation rate in wall-bounded flows. *J. Fluid Mech.*, 293:321–347.

[13] Jovanović, J., Ye, Q.-Y., Jakirlić, S. & Durst, F. 1998 Turbulence closure for the dissipation rate correlation. *Submitted to J. Fluid Mech.*

[14] Kawamura, H., Ohsaka, K. 1997 DNS of turbulent heat transfer in channel flow with low to medium-high Prandtl number fluid. In *Proc. 11th Symposium on Turbulent Shear Flows*, Vol. 1, pages 8.7-8.12, Grenoble, France.

[15] Kolovandin, B.A. & Vatutin, I.A. 1972 Statistical transfer theory in non-homogeneous turbulence. *Int. Journal of Heat and Mass Transfer*, 15:2371–2383.

[16] Koschmieder, E.L. 1993 Bénard Cells and Taylor Vortices. Cambridge University Press.

[17] Kulacki, F.A. & Richards, D.E. 1985 Natural Convection in plane layers and cavities with volumetric energy sources. In *Natural Convection: Fundamentals and Applications* Eds.: S. Kakac, W. Aung, and R. Viskanta, Springer, pp. 179-255.

[18] Lumley, J. 1978 Computational modeling of turbulent flows. *Advances in Applied Mechanics*, 18:123–176.

[19] Lumley, J. & Newman, G. 1977 The return to isotropy of homogeneous turbulence. *J. Fluid Mech.*, 82:161–178.

[20] Mansour, N.N., Kim, J. & Moin, P. 1988 Reynolds-stress and dissipation-rate budgets in a turbulent channel flow. *J. Fluid Mech.*, 194:15–44.

[21] Rodi, W., 1980 *Turbulence models and their application in hydraulics - a state of the art review.* IAHR-Publication, Delft, the Netherlands.

[22] Schmidt, M., Wörner, M. & Grötzbach, G. 1997 Direkte numerische Simulation der Konvektion in einer Fluidschicht mit interner Wärmequelle. *Forschungszentrum Karlsruhe, FZKA 5916.*

[23] Shikazono, N. & Kasagi, N. 1993 Modeling Prandtl number influence on scalar transport in isotropic and sheared turbulence. In *Proc. 9th Symp. on Turbulent Shear Flows*, pages 18.3.1–18.3.6, Kyoto, Japan.

[24] Tennekes, H. & Lumley, J.L., 1972 *A First Course in Turbulence.* The MIT Press, Cambridge, Mass.

[25] Willerding, G. & Baumann, W. 1996 FLUTAN 2.0 Input Specifications. Forschungszentrum Karlsruhe, FZKA 5712.

[26] Wörner, M. & Grötzbach, G. 1993 Turbulent heat flux balance for natural convection in air and sodium analysed by direct numerical simulations. In *Proc. 5th Int. Symp. on Refined Flow Modelling and Turbulence Measurements*, pp. 335–342, Paris, France.

[27] Wörner, M. 1994 *Direkte Simulation turbulenter Rayleigh-Bénard-Konvektion in flüssigem Natrium.* PhD thesis, Universität Karlsruhe (TH), KfK 5228.

[28] Wörner, M. & Grötzbach, G. 1995 Analysis of thermal variance equation for natural convection of air and sodium. In *Turbulence, Heat and Mass Transfer 1*, Eds.: K. Hanjalić and J.C.F. Pereira, pp. 332–337, Begell House.

[29] Wörner, M. & Grötzbach, G. 1995 Modelling the molecular terms in the turbulent heat flux equation for natural convection. In *Proceedings Tenth Symposium on Turbulent Shear Flows*, State College PA, USA, Volume 2, pages P2.73-P2.78.

[30] Wörner, M., Schmidt, M. & Grötzbach, G. 1997 DNS of turbulence in an internally heated convective fluid layer and implications for statistical modelling. *Journal of Hydraulic Research*, 35:773–797.

[31] M. Wörner & G. Grötzbach
DNS database of turbulent natural convection in horizontal fluid layers.
http://hbksun17.fzk.de:8080/IRS/eng/IRS3/TURBIT_DNS_database.html.

[32] Ye, Q.-Y., 1996 *Die turbulente Dissipation mechanischer Energie in Scherschichten.* PhD thesis, Universität Erlangen-Nürnberg.

Appendix: Transport equation for the heat flux dissipation term $\epsilon_{i\theta}$

For incompressible buoyant flow with the use of the Boussinesq approximation the equations for fluctuating velocity and fluctuating temperature read as follows:

$$\frac{\partial u_i}{\partial t} + U_k \frac{\partial u_i}{\partial x_k} + u_k \frac{\partial U_i}{\partial x_k} + \frac{\partial u_i u_k}{\partial x_k} - \frac{\partial \overline{u_i u_k}}{\partial x_k} + \beta\theta g_i = -\frac{1}{\rho}\frac{\partial p}{\partial x_i} + \nu \Delta_x u_i, \tag{A.1}$$

$$\frac{\partial \theta}{\partial t} + U_k \frac{\partial \theta}{\partial x_k} + u_k \frac{\partial \Theta}{\partial x_k} + u_k \frac{\partial \theta}{\partial x_k} = \alpha \Delta_x \theta. \tag{A.2}$$

To derive the equation for $\epsilon_{i\theta}$, first equations (A.1) and (A.2) are differentiated by $\partial/\partial x_l$:

$$\begin{aligned} \frac{\partial}{\partial t}\frac{\partial u_i}{\partial x_l} &+ \frac{\partial U_k}{\partial x_l}\frac{\partial u_i}{\partial x_k} + U_k \frac{\partial^2 u_i}{\partial x_k \partial x_l} + \frac{\partial u_k}{\partial x_l}\frac{\partial U_i}{\partial x_k} + u_k \frac{\partial^2 U_i}{\partial x_k \partial x_l} \\ &+ \beta g_i \frac{\partial \theta}{\partial x_l} + \frac{\partial^2}{\partial x_k \partial x_l}(u_i u_k - \overline{u_i u_k}) = -\frac{1}{\rho}\frac{\partial^2 p}{\partial x_i \partial x_l} + \nu \frac{\partial}{\partial x_l}\Delta_x u_i, \end{aligned} \tag{A.3}$$

$$\begin{aligned} \frac{\partial}{\partial t}\frac{\partial \theta}{\partial x_l} &+ \frac{\partial U_k}{\partial x_l}\frac{\partial \theta}{\partial x_k} + U_k \frac{\partial^2 \theta}{\partial x_k \partial x_l} + \frac{\partial u_k}{\partial x_l}\frac{\partial \Theta}{\partial x_k} + u_k \frac{\partial^2 \Theta}{\partial x_k \partial x_l} \\ &+ \frac{\partial}{\partial x_l}(u_k \frac{\partial \theta}{\partial x_k}) = \alpha \Delta_x \frac{\partial \theta}{\partial x_l}. \end{aligned} \tag{A.4}$$

Multiplying equation (A.3) by $\partial\theta/\partial x_l$ and equation (A.4) by $\partial u_i/\partial x_l$, one obtains:

$$\begin{aligned} &\frac{\partial \theta}{\partial x_l}\frac{\partial}{\partial t}\frac{\partial u_i}{\partial x_l} + \frac{\partial \theta}{\partial x_l}\frac{\partial u_i}{\partial x_k}\frac{\partial U_k}{\partial x_l} + U_k \frac{\partial \theta}{\partial x_l}\frac{\partial^2 u_i}{\partial x_k \partial x_l} + \frac{\partial \theta}{\partial x_l}\frac{\partial u_k}{\partial x_l}\frac{\partial U_i}{\partial x_k} + u_k \frac{\partial \theta}{\partial x_l}\frac{\partial^2 U_i}{\partial x_k \partial x_l} \\ &+ \beta g_i \frac{\partial \theta}{\partial x_l}\frac{\partial \theta}{\partial x_l} + \frac{\partial \theta}{\partial x_l}\frac{\partial^2}{\partial x_k \partial x_l}(u_i u_k - \overline{u_i u_k}) \\ &= -\frac{1}{\rho}\frac{\partial \theta}{\partial x_l}\frac{\partial^2 p}{\partial x_i \partial x_l} + \nu \frac{\partial \theta}{\partial x_l}\Delta_x \frac{\partial u_i}{\partial x_l}, \end{aligned} \tag{A.5}$$

$$\begin{aligned} &\frac{\partial u_i}{\partial x_l}\frac{\partial}{\partial t}\frac{\partial \theta}{\partial x_l} + \frac{\partial \theta}{\partial x_k}\frac{\partial u_i}{\partial x_l}\frac{\partial U_k}{\partial x_l} + U_k \frac{\partial u_i}{\partial x_l}\frac{\partial^2 \theta}{\partial x_k \partial x_l} + \frac{\partial u_i}{\partial x_l}\frac{\partial u_k}{\partial x_l}\frac{\partial \Theta}{\partial x_k} + u_k \frac{\partial u_i}{\partial x_l}\frac{\partial^2 \Theta}{\partial x_k \partial x_l} \\ &+ \frac{\partial u_i}{\partial x_l}\frac{\partial}{\partial x_l}(u_k \frac{\partial \theta}{\partial x_k}) = \alpha \frac{\partial u_i}{\partial x_l}\Delta_x \frac{\partial \theta}{\partial x_l}. \end{aligned} \tag{A.6}$$

Adding equation (A.5) and (A.6) and using the mass conservation law results in the following equation:

$$\frac{\partial}{\partial t}(\frac{\partial \theta}{\partial x_l}\frac{\partial u_i}{\partial x_l}) + 2\frac{\partial \theta}{\partial x_l}\frac{\partial u_i}{\partial x_k}\frac{\partial U_k}{\partial x_l} + U_k \frac{\partial}{x_k}(\frac{\partial \theta}{\partial x_l}\frac{\partial u_i}{\partial x_l}) + \frac{\partial \theta}{\partial x_l}\frac{\partial u_k}{\partial x_l}\frac{\partial U_i}{\partial x_k}$$

$$
\begin{aligned}
&+\frac{\partial u_i}{\partial x_l}\frac{\partial u_k}{\partial x_l}\frac{\partial \Theta}{\partial x_k}+u_k\frac{\partial \theta}{\partial x_l}\frac{\partial^2 U_i}{\partial x_k \partial x_l}+u_k\frac{\partial u_i}{\partial x_l}\frac{\partial^2 \Theta}{\partial x_k \partial x_l}+\beta g_i\frac{\partial \theta}{\partial x_l}\frac{\partial \theta}{\partial x_l}\\
&+\frac{\partial u_k}{\partial x_l}\frac{\partial u_i}{\partial x_k}\frac{\theta}{\partial x_l}+u_k\frac{\partial \theta}{\partial x_k}\frac{\partial u_i}{\partial x_l}+u_k\frac{\partial \theta}{\partial x_l}\frac{\partial^2 u_i}{\partial x_k \partial x_l}-\frac{\partial \theta}{\partial x_l}\frac{\partial^2}{\partial x_k \partial x_l}\overline{u_i u_k}\\
&=-\frac{1}{\rho}\frac{\partial \theta}{\partial x_l}\frac{\partial^2 p}{\partial x_i \partial x_l}+\nu\frac{\partial \theta}{\partial x_l}\Delta_x\frac{\partial u_i}{\partial x_l}+\alpha\frac{\partial u_i}{\partial x_l}\Delta_x\frac{\partial \theta}{\partial x_l}. \qquad \text{(A.7)}
\end{aligned}
$$

Considering the transformation

$$
\nu\frac{\partial \theta}{\partial x_l}\Delta_x\frac{\partial u_i}{\partial x_l}=\nu\Delta_x(\frac{\partial \theta}{\partial x_l}\frac{\partial u_i}{\partial x_l})-\nu\frac{\partial u_i}{\partial x_l}\Delta_x\frac{\partial \theta}{\partial x_l}-2\nu\frac{\partial^2 \theta}{\partial x_m \partial x_l}\frac{\partial^2 u_i}{\partial x_m \partial x_l}, \qquad \text{(A.8)}
$$

multiplying Eq. (A.7) by $(\nu+\alpha)$ and averaging Eq. (A.7), the exact equation for determining the dissipation term $\epsilon_{i\theta}$ is obtained:

$$
\begin{aligned}
&\frac{\partial \epsilon_{i\theta}}{\partial t}+U_k\frac{\partial \epsilon_{i\theta}}{\partial x_k}=-2(\nu+\alpha)\overline{\frac{\partial \theta}{\partial x_l}\frac{\partial u_i}{\partial x_k}}\frac{\partial U_k}{\partial x_l}-(\nu+\alpha)\overline{\frac{\partial \theta}{\partial x_l}\frac{\partial u_k}{\partial x_l}}\frac{\partial U_i}{\partial x_k}\\
&-(\nu+\alpha)\overline{\frac{\partial u_i}{\partial x_l}\frac{\partial u_k}{\partial x_l}}\frac{\partial \Theta}{\partial x_k}-(\nu+\alpha)\overline{u_k\frac{\partial \theta}{\partial x_l}}\frac{\partial^2 U_i}{\partial x_k \partial x_l}-u_k\frac{\partial u_i}{\partial x_l}\frac{\partial^2 \Theta}{\partial x_k \partial x_l}\\
&\underbrace{-\beta g_i(\nu+\alpha)\overline{\frac{\partial \theta}{\partial x_l}\frac{\partial \theta}{\partial x_l}}}_{T_1}-(\nu+\alpha)\overline{\frac{\partial u_k}{\partial x_l}\frac{\partial u_i}{\partial x_k}\frac{\partial \theta}{\partial x_l}}-(\nu+\alpha)\overline{u_k\frac{\partial \theta}{\partial x_k}\frac{\partial u_i}{\partial x_l}}\\
&-(\nu+\alpha)\overline{u_k\frac{\partial \theta}{\partial x_l}\frac{\partial^2 u_i}{\partial x_l \partial x_k}}-\frac{1}{\rho}(\nu+\alpha)\overline{\frac{\partial \theta}{\partial x_l}\frac{\partial^2 p}{\partial x_i \partial x_l}}+\underbrace{(\nu+\alpha)(\alpha-\nu)\overline{\frac{\partial u_i}{\partial x_l}\Delta_x\frac{\partial \theta}{\partial x_l}}}_{T_2}\\
&-2\nu(\nu+\alpha)\overline{\frac{\partial^2 u_i}{\partial x_l \partial x_m}\frac{\partial^2 \theta}{\partial x_l \partial x_m}}+\nu\Delta_x\epsilon_{i\theta}. \qquad \text{(A.9)}
\end{aligned}
$$

This equation is more complicated than the equation for ϵ. Until now $\epsilon_{i\theta}$ is usually modelled by using a simple form with empirical parameters. However, one should try to ensure that the proposed form is a physically plausible substitute for the real process. Looking into the term T_2, one obtains that $\overline{\frac{\partial \theta}{\partial x_l}\frac{\partial u_i}{\partial x_l}}$ depends also on the fluid Prandtl number, if $\alpha \neq \nu$. Therefore, for $Pr \neq 1$ a Prandtl number influence should be incorporated into the model for $\overline{\frac{\partial \theta}{\partial x_l}\frac{\partial u_i}{\partial x_l}}$. The correlation $\alpha\overline{\frac{\partial \theta}{\partial x_l}\frac{\partial \theta}{\partial x_l}}$ which represents the temperature dissipation ϵ_θ in the transport equation for $\overline{\theta^2}$ appears also in the term T_1 in Eq. (A.9). It seems that in future, analyses for every term in Eq. (A.9) should be carried out in detail in order to obtain a more accurate model for $\epsilon_{i\theta}$.